# Interaction coefficients in FCC nickel crystal identified from Berkovich nanoindentation imprints using FEMU

Alexandre Bourceret<sup>a,b,\*</sup>, Yves Gaillard<sup>a</sup>, Arnaud Lejeune<sup>a</sup>, Fabrice Richard<sup>a,\*\*</sup>

#### Abstract

Crystal plasticity models establish connections between macroscopic observations and microscopic plasticity mechanisms. However, the scale disparity between observables and underlying plasticity mechanisms complicates the estimation of certain material parameters, particularly slip system interaction coefficients. To bridge the gap between observations and plastic deformation mechanisms, Berkovich nanoindentation residual topographies can be used as observables for identifying crystal plasticity parameters. This study focuses on simultaneously identifying slip system interaction coefficients through an inverse approach using Berkovich nanoindentation topographies. We first establish an experimental database of residual topographies. Then, guided by a local a priori identifiability analysis, we select optimal experiments to identify all workhardening parameters. The parametric identification employs the finite element model updating (FEMU) method, followed by a posteriori validation to assess solution stability and experimental-numerical correspondence. The results reveal a distinct hierarchy of interaction coefficients, characterized by stronger sessile and weaker glissile interactions.

Keywords: Slip system interactions, Berkovich nanoindentation, Crystal plasticity, Inverse method

#### Introduction

Single crystal behavior laws are nowadays well established [1–4] and widely implemented in various finite element software, such as Zébulon, Cast3M, CalculiX and others [5–7]. Some implementations of the behavior laws have also been proposed as user material routines (UMAT) [8, 9], which can be used within structural mechanics software. An alternative is to use MFront [10], a numerical tool that allows to generate UMAT for different finite element software. However, using such constitutive laws requires a quantification of numerous material parameters [11–15]. Among these crystal plasticity parameters, quantifying the interactions between the different slip systems remains challenging [16–24].

<sup>\*</sup>Corresponding author

<sup>\*\*</sup>Corresponding author

In early models of crystal plasticity, latent hardening was defined as being equivalent to self hardening [25]. The first experimental characterization of interaction coefficients between slip systems was conducted by Franciosi et al. [26]. Two tensile tests were performed to sequentially activate selected slip systems. The interaction coefficients were estimated from the macroscopic tensile curves by calculating the ratio of the critical resolved shear stresses. However, ensuring that only the intended slip systems were activated remained difficult. This approach was applied to both compression and tensile tests, leading to different sets of values for the interaction coefficients [26–31]. In the early 2000s, discrete dislocation dynamics (DDD) enabled the simulation of the interaction between individual dislocations, allowing for the quantification of interaction coefficients [32, 33]. Nevertheless, the validation of these coefficients through a direct comparison of experimental and numerical dislocation structures presents considerable difficulty. Alternatively, the coefficients can be quantified by comparing the experimental and simulated responses of polycrystals under stress as in the works of Gérard et al. [34] or Guery et al. [20]. However, in studies involving polycrystalline samples, grain boundary behavior and slip transfer across grain boundaries must also be considered, which significantly complicates the identification and increases the number of parameters to be identified. In this context, given the diversity of interaction coefficient values reported in the literature, consensus sets of interaction coefficients are widely used [25, 35, 36].

In the early 2010s, the pile-up distribution around a residual imprint of indentation was found to be strongly dependent on the indented crystallographic orientation [37–40]. This has been confirmed for very distinct materials [41, 42]. Afterwards, several studies revealed the potential of single crystal indentation tests to extract not only hardness and elasticity, but also crystal plasticity parameters [37–39]. Renner et al. [21] showed that the residual imprint of a Berkovich indentation on a nickel single crystal is sensitive to all interaction coefficients. It suggests that the inverse analysis of nanoindentation imprints, using a crystal plasticity finite element model (FEM), can provide a precise quantification of crystal plasticity parameters, including the interaction coefficients. A significant advantage of nanoindentation tests is their ability to be performed within a single grain, even in polycrystalline samples. However, the existing literature on the application of the finite element model updating (FEMU) method to nanoindentation tests emphasizes the importance of carefully formulating the inverse problem, as different sets of parameters can yield identical responses [43–47]. To address this issue, an identifiability analysis must be conducted prior to the FEMU process to assess stability with respect to the chosen initial set of parameters (starting point) and the considered observables. The stability of the obtained solution of the inverse problem should also be evaluated after the FEMU process [48]. Renner et al. [22] showed that combining the Berkovich nanoindentation residual topographies from three representative orientations would be sufficient to identify 9 crystal plasticity parameters, including 6 interaction coefficients. Finite element simulations of the indentation of a single grain using a Berkovich tip require not only the crystallographic orientation of the grain but also the in-plane crystallographic orientation with respect to the tip [49]. Indeed, using such an indenter enhances the information contain in the residual imprints [21, 22], compared to the use of a self-similar axisymmetrical indenter [50]. However, this enhancement complicates the modeling process, which explains the scarcity of studies comparing experimental and numerical Berkovich indentation on the same crystallographic orientations [14].

The present study focuses on the simultaneous identification of 10 crystal plasticity parameters, including 7 interaction coefficients between slip systems, in FCC crystal. The first part presents the chosen material, polycrystalline nickel, and the experimental tests and measurements, including EBSD characterization of the indented grains, AFM topography measurements, nanoindentation tests, and tensile tests. The second part introduces the FEM of the Berkovich nanoindentation and tensile tests, including the size-independent crystal plasticity framework [51]. The model calibration method is also introduced in the second part. The third part presents the identifiability analysis used to carefully design the optimal experiments from the database established previously and also the methodology implemented for the identification of the targeted parameters. The starting point detailed in the third part comprises seven interaction coefficients obtained from the literature, and the remaining three work-hardening parameters are identified using the FEMU method on a tensile test curve of our nickel sample. The fourth part presents the identification process of these 10 crystal plasticity parameters. The obtained interaction coefficients are validated in the fifth part and compared with literature values.

# 1. Experimental tests and measurements

The material used in this study is a nickel polycrystal sourced from a cast ingot of 99.9% pure nickel, supplied by Goodfellow Cambridge Ltd. To promote the growth of larger grains (with diameters exceeding 100  $\mu$ m) and reduce dislocation density, the sample is annealed at 870°C for 3 hours. The materials were supplied as a cylindrical bar with a diameter of 20.6 mm. A cylindrical sample is cut from the bar for nanoindentation experiments (1 cm in height and 2.6 cm in radius), and the tensile test specimen is machined from the same bar (specimen illustrated in fig. I.1a). Nanoindentation tests are performed within individual grains of the sample, with a maximum indentation depth of 900 nm, while the second specimen undergoes tensile testing up to 15% strain. Details of the tensile test procedure and specimen geometry are provided in [21, 52], and are also summarized in appendix I. EBSD measurements are then performed to characterize the microstructure of the sample. Grains are selected from the characterized microstructure, and nanoindentation tests are subsequently performed within these grains. Finally, the residual topographies are measured by AFM.

#### 1.1. EBSD measurements

EBSD measurements are conducted to map a 1 mm<sup>2</sup> area of the sample top surface. The surface is polished using colloidal silica to improve the quality of the EBSD measurements and nanoindentation tests. The measurement is performed using a JEOL JSM 7600F scanning electron microscope coupled with an Ametek EDAX DigiView 5 for texture characterization.

The EBSD map was reconstructed using MTEX software [53, 54]. Grains were distinguished by applying a misorientation threshold of 5° between adjacent pixels. Based on the microstructure shown in fig. 1a, 11 grains are selected for nanoindentation. These grains are selected according to two criteria: their area, which is chosen to be as large as possible to minimize boundary effects during

indentation, and their orientation heterogeneity, which is maximized to ensure a diverse and representative database. In fig. 1a, the selected grains are colored according to their mean orientation [55], while the remaining grains are displayed in grey. The mean radius of the selected grains, approximated by a spherical shape, is  $R_{mean} = 131.8 \, \mu \text{m}$ , with a minimum radius of  $R_{min} = 80.7 \, \mu \text{m}$  (grain 5) and a maximum radius of  $R_{max} = 186.3 \, \mu \text{m}$  (grain 11). A cube-shaped graphic is overlaid on each selected grain to represent its mean orientation.

In fig. 1b, the colored dots represent all the pixels within the selected grains, while the black dot indicates the mean orientation calculated for each grain. A significant dispersion in orientation, reaching up to 14°, is observed for the grain 11, despite the small misorientation threshold used to define grain boundaries.

Table 1: Mean orientations of selected grains and azimuth angle from EBSD measurements. Euler's angles  $(\phi_1, \psi, \phi_2)$  in Bunge's convention (ZXZ) and Miller indices (hkl)[uvw], are obtained from EBSD measurements for the mean orientations of the grains. The (hkl) indices represent the orientation of the indented plane in the crystal reference frame, while [uvw] corresponds to the in-plane orientation. The azimuth angle  $\alpha$  defines the relative orientation between the crystal and a non-axisymmetric indenter. It is measured as the angle between the projection of the  $\overrightarrow{X}_{Crystal}$  axis of the crystal coordinate system onto the indentation plane and one of the symmetry axes of the indenter. This angle is illustrated in the central column of fig. 2, fig. 3, and fig. 4.

Grains	0. (9)	Eul	er's Angl	Miller indices						
Grams	α (°)	$\phi_1$ (°)	$\psi$ (°)	$\phi_2$ (°)	(hkl)			[uvw]		,]
1	164.35	148.36	48.66	245.28	-11	-5	11	12	-11	7
2	322.94	321.71	16.40	75.81	3	1	11	9	-7	-2
3	272.04	8.06	45.95	329.81	-5	9	10	9	4	1
4	96.76	80.76	40.92	310.58	-6	5	9	11	-6	11
5	163.10	147.14	34.32	195.39	1	-4	6	9	2	3
6	12.20	65.42	1.59	290.78	0	0	1	12	1	0
7	8.08	352.08	38.36	5.12	1	8	10	12	0	-1
8	129.01	293.01	16.04	89.57	2	0	7	7	-3	-2
9	165.29	345.77	5.81	343.60	0	1	10	12	7	0
10	164.84	219.54	28.04	111.65	5	-2	10	8	5	-3
11	291.84	3.83	30.14	2.32	0	7	12	10	-1	0

The mean orientations, expressed as Euler's angles and computed using MTEX, are presented in table 1 following Bunge's convention. The table 1 also includes the Miller indices of each grain. In the crystal reference frame, the (hkl) direction corresponds to the axis perpendicular to the indentation plane, while the [uvw] direction represents the in-plane axis of each grain. Table 1 also provides the azimuth angle  $\alpha$ , defined by Renner et al. [22]. This angle quantifies the relative orientation between the crystal and a non-axisymmetric indenter. It is defined as the angle between the projection of  $\overrightarrow{X}_{Crystal}$  axis of the crystal coordinate system onto the indentation plane, and one of the symmetry axes of the indenter. Two of these axes,  $\overrightarrow{X}_{Crystal}$  and  $\overrightarrow{Y}_{Crystal}$ , are represented on top of the experimental topographies, along with the indenter, in the middle column of the fig. 2, fig. 3, and fig. 4.

# 1.2. Nanoindentation tests

The nanoindentation tests are conducted using an Anton Paar ultra nano hardness tester (UNHT). All tests are performed at room temperature and hu-

midity, using a diamond Berkovich tip with a tip radius of about 110 nm. Displacement controlled tests are carried out to a maximum depth of 900 nm. The resulting indentation curves obtained for the selected grains are given in appendix II.

#### 1.3. AFM measurements

The AFM measurements are performed using a Park PSIA XE-150. The dimensions of the AFM maps in the indentation plane are set to  $20 \times 20~\mu\text{m}^2$ , ensuring that the edge length of the scanned area is more than twenty times the maximum indentation depth. The measurements are processed using WSxM software [56]. The topography data processing involves a global plane interpolation, which is applied uniformly to each measured topography, followed by a flatten, performed from the topography edges. This WSxM processing corrects the non-flatness of the sample's top surface, and the same treatment is applied to all topographies. Artifacts, such as surface debris, are removed during post-treatment using MATLAB. The resulting experimental imprints are illustrated in fig. 2, fig. 3, and fig. 4, as shown in the central column. As expected, the pileup distribution shows strong dependence on the crystallographic orientation of the indented grains.

#### 2. Numerical modeling and calibration

#### 2.1. Single crystal plasticity framework

A general framework for finite strain elasto-viscoplastic behavior is employed to describe the crystal plasticity behavior. The deformation gradient is split into its elastic part  $\overline{\overline{F}}_{e}$  and viscoplastic part  $\overline{\overline{F}}_{vp}$ , following the approach introduced by Lee [57]:

$$\overline{\overline{F}} = \overline{\overline{F}}_e \cdot \overline{\overline{F}}_{vp}. \tag{1}$$

The Green-Lagrange strain  $\overline{\overline{E}}$  is obtained from the elastic part  $\overline{\overline{F}}_e$  of the deformation gradient:

$$\overline{\overline{E}} = \frac{1}{2} \left[ \overline{\overline{F}}_e^T \cdot \overline{\overline{F}}_e - \overline{\overline{I}} \right]. \tag{2}$$

Given the high stacking fault energy of the nickel (125 mJ · m<sup>-2</sup> for our specimen [52]), its tendency to produce twinning defects during hardening is low. Therefore, it is assumed that the plastic deformation occurs solely on the 12 FCC slip systems  $\{111\}\langle110\rangle$ . The evolution of plastic deformation is described by a cumulative shear strain rate across all slip systems [58]:

$$\dot{\overline{F}}_{vp} \cdot \overline{\overline{F}}_{vp}^{-1} = \sum_{s=1}^{12} \dot{\gamma}^s \overline{\overline{N}}^s, \text{ with } \overline{\overline{N}}^s = \overrightarrow{l}^s \otimes \overrightarrow{n}^s,$$
 (3)

where  $l^s$  is the slip direction,  $n^s$  is the normal of the slip plane, and  $\dot{\gamma}^s$  is the shear strain rate.  $\overline{\overline{N}}^s$  denotes the Schmid tensor on the s-th given slip system [59]. The shear strain rate is defined based on a size-independent crystal plasticity laws following a Norton flow rule with threshold [60]:

$$\dot{\gamma}^s = \left\langle \frac{|\tau^s| - \tau_0 - R^s}{K} \right\rangle^n \frac{\tau^s}{|\tau^s|},\tag{4}$$

where  $\tau^s$  is the resolved shear stress on the s-th given slip system and  $\tau_0$  represents the critical resolved shear stress. The term  $R^s$  accounts for the isotropic hardening on each slip system, while K and n govern the viscosity response of the material. The resolved shear stress  $\tau^s$  is a scalar variable defined as:

$$\tau^s = \overline{\overline{M}} : \overline{\overline{N}}^s, \text{ with } \overline{\overline{M}} = \overline{\overline{F}}_e^T \cdot \overline{\overline{F}}_e \cdot \left(\overline{\overline{\overline{C}}} : \overline{\overline{E}}\right),$$
(5)

where  $\overline{M}$  denotes the Mandel stress tensor, projected onto each slip systems through the Schmid tensor  $\overline{\overline{N}}^s$ . The stiffness tensor is denoted by  $\overline{\overline{C}}$ . The Mandel stress  $\overline{\overline{M}}$  is related to the Cauchy stress  $\overline{\overline{\sigma}}$  as follows:

$$\overline{\overline{\sigma}} = \frac{1}{J_e} \overline{\overline{F}}_e^{-T} \cdot \overline{\overline{M}} \cdot \overline{\overline{F}}_e^T, \tag{6}$$

where  $J_e$  denotes the determinant of the elastic part  $\overline{\overline{F}}_e$  of the deformation gradient.

Hysteresis loops during unloading/reloading cycles indicate the presence of kinematic hardening [61]. However, such hysteresis loops are not observed in the present study for any crystallographic orientation. Based on this observation, it is assumed that each slip system undergoes purely isotropic hardening. The isotropic hardening of each slip system is described by a Voce law, incorporating the interaction matrix as proposed by Méric et al. [51]:

$$R^{s} = Q \sum_{r} h^{sr} \left( 1 - e^{-b|\gamma^{r}|} \right), \tag{7}$$

where Q drives the hardening saturation and b drives the rate of saturation, and [h] the interaction matrix. For the nickel FCC sample under consideration, [h] is a  $12 \times 12$  matrix that defines the hardening interactions between the slip systems. The interaction matrix used in this study is presented in table 2, incorporating 7 interaction coefficients, as proposed by Madec and Kubin [62]. The interaction coefficients are listed in table 3, along with the geometric relationships between the normal vectors of the slip planes and slip directions of the two interacting slip systems corresponding to each interaction.

The anisotropic elastic behavior is described by 3 parameters ( $c_{11}$ ,  $c_{12}$ , and  $c_{44}$ ), which are the independent components of the stiffness tensor in eq. (5) for FCC material. The viscosity is described through 2 parameters (K and n) in eq. (4). The present study focuses on identifying the interactions between slip systems, which are part of isotropic hardening and cannot be identified independently from the other parameters controlling hardening. Therefore, the 10 parameters targeted for identification in this study are listed below:

$$\{\theta\} = \{Q, b, \tau_0, h_1, h_2, h_3, h_4, h_5, h_6, h_7\} \tag{8}$$

Consequently, the single crystal plasticity hardening behavior is governed by 10 plastic parameters  $(Q, b, \tau_0, \text{ and } h_{i=1,...,7})$  in eqs. (4) and (7).

Table 2: Interaction matrix in the Schmid and Boas convention [59], as defined by Franciosi [63], and adapted following Madec and Kubin [62, 64].

	$s \backslash r$	B2	B4	B5	C1	C3	C5	A2	A3	A6	D1	D4	D6
	B2	$h_1$	$h_2$	$h_2$	$h_3$	$h_6$	$h_5$	$h_4$	$h_7$	$h_7$	$h_3$	$h_5$	$\overline{h_6}$
	B4	$h_2$	$h_1$	$h_2$	$h_6$	$h_3$	$h_5$	$h_5$	$h_3$	$h_6$	$h_7$	$h_4$	$h_7$
	B5	$h_2$	$h_2$	$h_1$	$h_7$	$h_7$	$h_4$	$h_5$	$h_6$	$h_3$	$h_6$	$h_5$	$h_3$
	C1	$h_3$	$h_6$	$h_5$	$h_1$	$h_2$	$h_2$	$h_3$	$h_5$	$h_6$	$h_4$	$h_7$	$h_7$
	C3	$h_6$	$h_3$	$h_5$	$h_2$	$h_1$	$h_2$	$h_7$	$h_4$	$h_7$	$h_5$	$h_3$	$h_6$
[ <i>h</i> ] _	C5	$h_7$	$h_7$	$h_4$	$h_2$	$h_2$	$h_1$	$h_6$	$h_5$	$h_3$	$h_5$	$h_6$	$h_3$
[h] =	A2	$h_4$	$h_7$	$h_7$	$h_3$	$h_5$	$h_6$	$h_1$	$h_2$	$h_2$	$h_3$	$h_6$	$h_5$
	A3	$h_5$	$h_3$	$h_6$	$h_7$	$h_4$	$h_7$	$h_2$	$h_1$	$h_2$	$h_6$	$h_3$	$h_5$
	A6	$h_5$	$h_6$	$h_3$	$h_6$	$h_5$	$h_3$	$h_2$	$h_2$	$h_1$	$h_7$	$h_7$	$h_4$
	D1	$h_3$	$h_5$	$h_6$	$h_4$	$h_7$	$h_7$	$h_3$	$h_6$	$h_5$	$h_1$	$h_2$	$h_2$
	D4	$h_7$	$h_4$	$h_7$	$h_5$	$h_3$	$h_6$	$h_6$	$h_3$	$h_5$	$h_2$	$h_1$	$h_2$
	D6	$h_6$	$h_5$	$h_3$	$h_5$	$h_6$	$h_3$	$h_7$	$h_7$	$h_4$	$h_2$	$h_2$	$h_1$

# 2.2. Finite element modeling of nanoindentation and tensile tests

The implementation of the behavior law in a FEM, as defined by eqs. (3) to (5) and (7), is detailed in [65] and [66]. The MFront numerical tool (version 3.3.3) is used to generate a UMAT for Ansys software (version 2022R1), which is subsequently used to simulate both nanoindentation and tensile tests.

The 3D FEM of the nanoindentation test is illustrated in fig. 5a. The model contains 23286 quadratic elements (C3D20R): 15000 elements representing the indented part of the grain, 7000 for the Berkovich tip and 1282 for the contact between the tip and the sample. Reduced integration is employed, resulting in each quadratic element having eight integration points. The contact problem is addressed using the Lagrange multipliers method for computing the normal force and the penalty method for the tangential force [67, 68]. The diamond tip is isotropic and elastic (Young's modulus E=1141 GPa and Poisson's ratio  $\nu=0.07$ ). The experimental indentation depth as a function of time is then used to impose the top of the tip displacement in the nanoindentation simulations. Friction tip/sample is modeled according to the Coulomb's law, with a coefficient  $\mu=0.2$ .

The dimensions of the cylindrical domain describing the sample and the indenter tip are chosen to prevent boundary effects. The dimensions are parameterized relative to the maximum indented depth  $h_{max}$ . The radius of the cylinder modeling the nickel sample is equal to its height  $R=h=60h_{max}$ , while the height of the indenter tip is similarly parameterized as  $h_{ind}=60h_{max}$ . For the indentation depth in this study, the radius of the cylinder, its height and that of the indenter ones are  $R=h=h_{ind}=54~\mu m$ . Regarding the sample boundary conditions, the lower surface of the cylinder is clamped while its lateral surface is free. The experimental displacement is applied to the upper surface, which is colored in blue in fig. 5a and defined as  $\overrightarrow{h}=-h_{exp}\overrightarrow{Y}_{Ansys}$ . Finally, the model consists of 282156 degrees of freedom, and one nanoindentation simulation requires approximately 6.3 hours on our computational facility using INTELMPI parallelization (2 Intel Xeon 2.70 GHz processors, each comprising 28 cores).

The FEM corresponding to the macroscopic tensile test is shown in fig. 5b.

Table 3: Slip system interactions and their geometric relationships between slip plane normal vectors and slip directions. The geometric relationship between the normal vectors to the slip planes and slip directions, which defined the interaction coefficients carried out in this study, is described as follows. s and r correspond to the slip system under consideration and the interacting slip systems, respectively.  $\overrightarrow{n}^s$  and  $\overrightarrow{l}^s$  refer to the normal vector of the slip plane and the slip direction, respectively.  $\overrightarrow{l_j}$  defines the interaction direction of the two interacting slip systems. Sessile interactions correspond to  $(h_3,h_6)$ , and glissile ones to  $(h_1,h_2,h_4,h_5,h_7)$ 

Name	Parameter	Geometric relations
Self-hardening	$h_1$	$\overrightarrow{n}^s = \overrightarrow{n}^r \text{ and } \overrightarrow{l}^s = \overrightarrow{l}^r$
Coplanar	$h_2$	$\overrightarrow{n}^s = \overrightarrow{n}^r \text{ and } \overrightarrow{l}^s \neq \overrightarrow{l}^r$
Hirth lock	$h_3$	$\overrightarrow{n}^s = \overrightarrow{n}^r \text{ and } \overrightarrow{l}^s \cdot \overrightarrow{l}^r = 0$
Colinear	$h_4$	$\overrightarrow{n}^s \neq \overrightarrow{n}^r \text{ and } \overrightarrow{l}^s = \overrightarrow{l}^r$
Glissile junction $G_{60^{\circ}}$	$h_5$	$\overrightarrow{n}^{s} \neq \overrightarrow{n}^{r} \text{ and } \overrightarrow{l}^{s} \neq \overrightarrow{l}^{r},$ $\cos^{-1}\left(\frac{\overrightarrow{l_{j}} \cdot \overrightarrow{l}^{s}}{\ \overrightarrow{l_{j}}\  \cdot \ \overrightarrow{l}^{s}\ }\right) = \frac{\pi}{3},$ $\overrightarrow{l}^{s} \cdot \overrightarrow{l}^{r} \neq 0,$ $\overrightarrow{l}^{s} \wedge \overrightarrow{l}^{r} = \begin{cases} \pm \overrightarrow{n}^{s} \\ \text{or} \\ \pm \overrightarrow{n}^{r} \end{cases}$
Lomer lock	$h_6$	$\overrightarrow{n}^s \neq \overrightarrow{n}^r, \overrightarrow{l}^s \neq \overrightarrow{l}^r, \overrightarrow{l}^s \cdot \overrightarrow{l}^r \neq 0,$ $\overrightarrow{l}^s \wedge \overrightarrow{l}^r = \begin{cases} \pm \overrightarrow{n}^s \\ \text{and} \\ \pm \overrightarrow{n}^r \end{cases}$
Glissile junction $G_{0^{\circ}}$	$h_7$	$\overrightarrow{n}^{s} \neq \overrightarrow{n}^{r} \text{ and } \overrightarrow{l}^{s} \neq \overrightarrow{l}^{r},$ $\cos^{-1}\left( \frac{\overrightarrow{l_{j}} \cdot \overrightarrow{l}^{s}}{\ \overrightarrow{l_{j}}\  \cdot \ \overrightarrow{l}^{s}\ } \right) = 0,$ $\overrightarrow{l}^{s} \cdot \overrightarrow{l}^{r} \neq 0,$ $\overrightarrow{l}^{s} \wedge \overrightarrow{l}^{r} = \begin{cases} \pm \overrightarrow{n}^{s} \\ \text{or} \\ \pm \overrightarrow{n}^{r} \end{cases}$

The model consists of 8000 linear elements (C3D8), following the approach used by Fivel and Forest [69]. According to Kraska et al. [70], quadratic elements are not necessary to accurately capturing the tensile curve. Each element is assigned a randomly chosen crystallographic orientation, allowing it to be treated as an individual grain. Regarding boundary conditions, the node at the origin is fixed, while all nodes on the surface  $S_b$  are constrained along the x axis. Additionally, the node at  $(0,0,z_{\text{max}})$  is constrained in y axis to prevent the rigid body rotation. Finally, the displacement  $\overrightarrow{U} = (U_x,0,0)$  is applied to the surface  $S_I$ . The displacement expression  $U_x$ , calculated from the experimental strain, is detailed by Renner et al. [71].

#### 2.3. Model calibration

Parametric quantification can be achieved through finite element model updating method (FEMU) [72]. The parameter estimation is obtained by mini-

mizing a cost function  $\omega$  that quantifies the experiment-simulation gap through adjustment of the target parameter set  $\{\theta\}$ . To guarantee that the cost function remains convex within the observable space, it is commonly formulated in a quadratic form [4, 13, 17, 73, 74]. In this study, the cost function is defined as:

$$\omega(\{\theta\}) = \frac{1}{2N} \sum_{j=1}^{M} \sum_{i=1}^{N} \left( \frac{\{\tilde{Z}_{num}(\{\theta\})\}_{i}^{j} - \{\tilde{Z}_{exp}\}_{i}^{j}}{\max_{i} \{\tilde{Z}_{exp}\}^{j}} \right)^{2},$$
(9)

where M is the number of considered topographies, and N is the number of acquisition points for each topography. Z represents the out-of-plane coordinates of the deformed surface in the indentation direction corresponding to the  $\overrightarrow{Y}_{Ansys}$  direction in fig. 5a. The cost function is normalized by both the number of points N and the maximal height of the topography. j denotes the index of the topographies, and i represents the i-th pixel of each topography. The numerical response  $\{\tilde{Z}_{num}(\{\theta\})\}^j$  of the j-th topography is compared to the corresponding experimental topography  $\{\tilde{Z}_{exp}\}^j$ . The experimental and numerical topographies are made dimensionless through the following expression:

$$\tilde{Z} = \frac{h_{max} + Z}{h_{max}}. (10)$$

This definition of height allow for greater weighting to be assigned to the pile-up in the identification process, as values greater than one correspond to points above the zero level of the topographies. All numerical topographies are interpolated onto the experimental measurement grid, ensuring they contain the same number of points N. The experimental topographies are described by a regular grid of  $512 \times 512$  pixel . These pixels are then reshaped into a vector, following the path illustrated in fig. 6a, with indices  $i \in \{1, ..., N\}$ .

During the FEMU process, the sensitivity of observables to parameters guides their evolution, as detailed in appendix III. The dimensionless sensitivity of the  $j^{th}$  dimensionless topography  $\tilde{Z}_{num}$  to the  $k^{th}$  parameter  $\theta_k$  is calculated as follows:

$$\bar{S}_{ik}^{j} = \frac{\theta_{k}}{\max_{i} \left\{ \tilde{Z}_{num} \left( \left\{ \theta \right\} \right) \right\}^{j} \sqrt{N}} \frac{\partial \left\{ \tilde{Z}_{num} \left( \left\{ \theta \right\} \right) \right\}_{i}^{j}}{\partial \theta_{k}}, \tag{11}$$

with  $k \in \{1, ..., N_{\theta}\}$ , where  $N_{\theta} = 10$  is the total number of parameters in this study, as reported in eq. (8). To incorporate multiple topographies in the identifiability analysis, their sensitivity matrices are concatenated, as shown in eq. (C.1).

The FEMU process is carried out using a toolchain consisting of 3 software products: MIC2M [75], MFront [10] and Ansys [6]. MIC2M pilots the minimization process of the cost function defined in eq. (9) using the selected topographies, as detailed in section 2.3 and appendix III. It governs the evolution of the parameters through iterations of a modified Levenberg-Marquardt algorithm [76], from the starting point to the solution, named  $\{\hat{\theta}\}$ . At each iteration, MIC2M passes the current material parameters  $\{\theta\}^{(k)}$  to MFront, which implements the behaviour law for the given parameter set  $\{\theta\}^{(k)}$ . MIC2M also provides MFront with the crystallographic orientation of the grain under consideration. The implementation of the behavior law using MFront is linked to Ansys, allowing the computation of the required variables at each integration point. Nanoindentation tests are then simulated for the parameter set

 $\{\theta\}^{(k)}$ , generating the indentation curves and topographies. This procedure is repeated  $N_{\theta}$  times for each topography to calculate the dimensionless local sensitivities (using eqs. (10), (11), (C.1) and (C.2)) of the topographies with respect to the parameter set  $\{\theta\}^{(k)}$ . Each parameter is perturbed by a fixed value of  $\varepsilon = 5 \times 10^{-3}$  for the sensitivity evaluation. If the *j*-th parameter is perturbed, then the perturbed value of the parameter is defined as  $\theta_j$   $(1 + \varepsilon)$ . Using these sensitivities, MIC2M calculates the updated parameter set  $\{\theta\}^{(k+1)}$  for the next iteration by eq. (C.3). Having introduced the numerical modeling and FEMU method, the following section presents the methodology used for parameter identification.

#### 3. Methodology

Identification of material parameters relies on resolving a well-posed inverse problem. Solving the inverse problem using the FEMU method involves reformulating it as a minimization problem. This can be expressed as follows:

$$\{\hat{\theta}\} = \underset{\{\theta\} \in \mathbb{R}^n}{\operatorname{argmin}} \ \omega\left(\{\theta\}\right),$$
 (12)

where  $\{\theta\}$  is the vector of the targeted parameters, and  $\{\hat{\theta}\}$  is the solution of the minimization process. The methodology for constructing a well-posed inverse problem is based on an a priori optimal experimental design. This involves selecting observable(s) that enable material parameter identification while ensuring maximum stability of the starting point for identification in section 2.3.

This selection of observables is made for two reasons. The first is computational time. On our computation facility, a single iteration of the cost function minimization algorithm would take approximately 32 days if all 11 grain observables were used (11 days × 11 parameters ×6.3 hours). Limiting the number of simulations in the FEMU process is therefore essential. Each additional observable increases the computation time by approximately 3 days per iteration. The second, and more critical, reason is the conditioning of the inverse problem. Adding more observables does not necessarily improve the conditioning and may even degrade it, as highlighted in prior studies [22, 74, 77]. For instance, Bolzon et al. [74] illustrates that incorporating an indentation curve into the imprint profile leads to poor conditioning of the inverse problem. Similar results are reported in the context of crystal plasticity, where the coupling between the indentation curve and residual topographies is investigated [22, 66]. Consequently, the present identifiability study and FEMU process focus exclusively on residual topographies, excluding indentation curves.

The algorithm used to solve the inverse problem [76, 78, 79] is capable of locating a local minimum near the specified starting point. However, it is crucial to ensure that the starting point is sufficiently close to the solution. To achieve this, the macroscopic plastic parameters  $\{Q, b, \tau_0\}$  are determined from a tensile test, while the interaction coefficients  $h_{i,i\in\{1,\dots,7\}}$  are obtained from DDD simulations for nickel, as reported in the literature [62]. The elastic constants,  $c_{11} = 248$  GPa,  $c_{12} = 153$  GPa, and  $c_{44} = 116$  GPa, are adopted from [80], and the viscosity parameters, K = 8 MPa.s<sup>1/n</sup> and n = 7, are taken from [21]. An a priori identifiability analysis is subsequently conducted using the complete experimental database described in section 1. The identifiability analysis is based

on the I-index, which evaluate the stability of a given point in the parameter space. Guided by the I-index, this section focuses on selecting the most relevant topography(ies) in conjunction with the predefined starting point. This section first introduces the identifiability analysis employed in this study, then defines the starting point for parameter identification. Finally, it presents the optimal experiment design obtained from this identifiability analysis.

#### 3.1. Local identifiability analysis

When using indentation curves, the non-uniqueness of the solution [81] has been linked to extreme sensitivity to the experimental errors [82]. Therefore, an identifiability analysis is conducted to ensure that the inverse problem defined in eq. (12) is locally not very sensitive to errors on the topographies used in the cost function. The identifiability analysis is then performed on the  $[\bar{G}]$  matrix, which is calculated from the concatenated sensitivity matrix of the topographies, as shown in eq. (C.2).

The conducted identifiability analysis evaluates both the sensitivity of the topographies to the parameters and the multicollinearity between their sensitivity vectors. This study utilizes the identifiability index (*I*-index) originally introduced by Richard et al. [83], which is defined as:

$$I_K = \log_{10} \left( \frac{\lambda_{max} \left( \left[ \bar{G} \right] \right)}{\lambda_{min} \left( \left[ \bar{G} \right] \right)} \right), \tag{13}$$

where  $\lambda_{max}$  and  $\lambda_{min}$  refers to the maximal and the minimal eigenvalue of  $[\bar{G}]$ , respectively. The common logarithm is later introduced to facilitate the interpretation of this identifiability index [84]. K denotes the set of parameters considered in the evaluation of the I-index, which is calculated from the sensitivity matrix truncated to retain only the columns corresponding to these parameters. The inverse problem is considered to be well-conditioned when the I-index is less than 2, and ill-conditioned when the I-index is greater than 3, as reported in the literature [85]. Between these values, the conditioning is moderate and requires further investigation. These values are associated with the shape of the cost function [21, 22, 48, 66, 76]. The I-index can be calculated a priori to FEMU process, allowing for the selection of an optimal set of experiments based on a defined starting point. Additionally, the I-index can also be calculated a posteriori to the FEMU process to assess the stability of the obtained solution.

The following section will undertake an a priori investigation of the conditioning of the inverse problem as a function of the selected observables and their combinations.

# 3.2. Definition of a starting point for the parameters

Based on the experimental macroscopic tensile behaviour of the sample illustrated in fig. I.1, 3 parameters  $\{Q, b, \tau_0\}$  are calibrated to establish the starting point for the FEMU process, i.e., the initial values of the material parameters. The remaining 7 parameters from the targeted set  $\{\theta\}$  in eq. (8) are fixed based on the literature [62, 64] and are summarized in table 4. The FEMU process is carried out using a numerical polycrystal, as described in section 2.2 and illustrated in fig. 5b. The FEMU approach is the same for the tensile curve

as it is for the topographies. With Z replaced by stress  $\sigma$  in eqs. (9) to (11), the cost function and sensitivity are expressed in terms of the observable tensile curve. The evolution of the parameters is also calculated using eq. (C.4). Finally, the red line in fig. I.1b represents the simulated curve using the identified parameters  $\{\hat{\theta}_{MK}\}$ , which shows good agreement with the experimental results.

Table 4: Starting point definition from identified and literature-based parameters. It is established by the identification of 3 plastic parameters using a tensile test curve, while 7 interaction coefficients are fixed based on values from the literature [62, 64], calculated using DDD simulations. A comparison between the experimental curve and numerical curves is illustrated in fig. I.1.

	Ide	entifi	ied	Literature-based							
Parameters	Q	b	$ au_0$	$h_1$	$h_2$	$h_3$	$h_4$	$h_5$	$h_6$	$h_7$	
	(MPa)	(-)	(MPa)	(-)	(-)	(-)	(-)	(-)	(-)	(-)	
$\{\hat{\theta}_{MK}\}$	140.7	8.0	27.0	0.35	0.35	0.21	0.82	0.30	0.41	0.32	

#### 3.3. Selection of the imprints based on a priori identifiability analysis

The aim is to select from the experimental database the optimal balance between the a priori identifiability of the given starting point with respect to the selected topography(ies) and the computational time of the FEMU process. To achieve this, the experimental database is explored using the I-index defined in eq. (13) as a decision-making tool to select the most relevant data. The database comprises residual topographies obtained after Berkovich nanoindentation tests, as illustrated in the central columns of figs. 2 to 4. Corresponding simulations of these topographies, generated using the starting point  $\{\hat{\theta}_{MK}\}$  (assumed to be close to the solution  $\{\hat{\theta}\}$ ), are presented in the right columns of figs. 2 to 4.

As a function of the spatial steps, the selected portion of the topography Zfollows a square spiral path from point B to point C, as shown in fig. 6. The considered part is shown in color in fig. 6a and in blue in fig. 6b, while the remaining portion of topography is depicted in black, white, and grey, respectively. The contact zone between the sample and the indenter, spanning from point A to point B in fig. 6, is excluded from the identifiability analysis and the FEMU process. This exclusion is due to inaccuracies in AFM experimental measurements within the imprint and possible numerical errors associated with contact modeling. The size of the square truncation in the center of the topography, as previously discussed by Renner et al. [22]. In this study, a similar central square truncation of  $230 \times 230$  pixel is employed. In addition, the edge of the topography, between points C and D, is also excluded due to an observed dilution of relevant information, characterized by an increase in the I-index in the majority of the grains. The edge truncation removes half of the remaining pixel after the center truncation. The size of the edge truncation is carefully chosen to eliminate regions with increase in the I-index values while retaining most of the pile-ups, as shown in figs. 6 and 9. The combined truncations result in the exclusion of an area equivalent to a  $320 \times 320$  pixel square. Finally, 39%of each topography is retained for analysis. This selected part contains the most relevant information, particularly the regions where the pile-ups are.

#### 3.3.1. Identifiability analysis using a single topography

The study examines whether the material parameters can be identified from a single topography. Three cases are analyzed: the identifiability of only the 3 hardening parameters  $\{Q, b, \tau_0\}$ , the identifiability of only the 7 interaction coefficients  $h_{i,i\in\{1,\dots,7\}}$ , and the identifiability of all 10 targeted plastic parameters. The identifiability results are presented in table 5 for all the indented grains, with mean orientations listed in table 1, using the starting point  $\{\hat{\theta}_{MK}\}$  defined in table 4. The evolution of the *I*-index is shown as a function of the spatial steps k, normalized by the number of the pixels N between point B and C, as illustrated in fig. 7.

Table 5: Identifiability outcomes using a single topography. The I-index is calculated for the 3 parameter sets K under consideration. The identifiability analysis is conducted using the starting point,  $\{\hat{\theta}_{MK}\}$ , defined in section 3.2. For the inverse problem, the color green denotes good conditioning, orange indicates average conditioning, and red signifies ill conditioning.

Grains		$I_K$	
Grains	$K = \{Q, b, \tau_0\}$	$K = \{h_{i,i \in \{1,\dots,7\}}\}\$	$K = \{\hat{\theta}_{MK}\}$
1	2.2	1.8	4.0
2	1.9	2.2	2.8
3	2.2	1.7	3.9
4	1.9	1.6	3.4
5	1.6	2.4	3.2
6	2.3	1.6	2.9
7	2.4	3.5	3.8
8	2.2	1.3	2.9
9	2.3	3.0	2.9
10	1.6	1.4	3.0
11	2.2	1.6	3.7

For the triplet  $\{Q, b, \tau_0\}$ , all identifiability indices  $I_{\{Q,b,\tau_0\}}$  in table 5 are less than 2.5, ranging from 1.6 for grains 5 and 10, to 2.4 for grain 7. For grains 2, 4, 5 and 10, the I-index values are less than 2, indicating a well-conditioned inverse problem when identifying only the 3 hardening parameters  $\{Q, b, \tau_0\}$  using one of these topographies.

For the 7 interaction coefficients,  $I_{\{h_{i,i}\in\{1,\dots,7\}}$  values range from 1.3 (grain 8) to 3.5 (grain 7). These results indicate a significant disparity in the relevant information contained in the different topographies regarding the interaction coefficients. 7 out of the 11 topographies have  $I_{\{h_{i,i}\in\{1,\dots,7\}\}}$  values less than 2. Therefore, provided the triplet  $\{Q,b,\tau_0\}$  is known, it is possible to identify all the interaction coefficients from a single topography by choosing a suitable crystal orientation.

Notably, only one topography is required to identify either the triplet  $\{Q, b, \tau_0\}$  or the septuplet  $\{h_{i,i\in\{1,\dots,7\}}\}$ . However, the *I*-index for the 3 hardening parameters are higher than for the 7 interaction coefficients (grains 1, 3, 4, 6, 8, 10 and 11). These results confirm the high relevance of the information contained in these topographies for identifying the interaction coefficients.

The difficulty arises in simultaneously identifying all 10 parameters, as the I-index values are superior to 2.5 for all the selected grains. A single topography is not sufficient to identify all the 10 targeted parameters simultaneously, in

agreement with the results of Renner et al. [22]. Consequently, the following section explores the combination of topographies.

#### 3.3.2. Identifiability analysis using multiple topographies

The combinations of 2 and 3 topographies are investigated to improve the conditioning of the inverse problem. When combining 2 and 3 topographies, 55 pairs and 165 triplets, respectively, can be generated from the 11 topographies. It is important to note that permutations of topographies yield the same final I-index value. The results for the combinations of 2 topographies are presented in table 6, showing the I-index values calculated for all the 10 targeted parameters, as well as for the 7 interaction coefficients only. In table 6, two cases are analyzed: the identifiability of only the 7 interaction coefficients  $h_{i,i\in\{1,\ldots,7\}}$ , and the identifiability of all 10 targeted plastic parameters. For 3 topographies, the results are provided in tables IV.1 and IV.2 of appendix IV, only for the 10 targeted parameters.

Table 6: Identifiability outcomes using combinations of 2 topographies. The I-index is computed for 2 parameter sets, K, using combinations of 2 topographies. The values in the lower triangular portion of the table correspond to parameter set  $K = \{h_{i,i \in \{1,...,7\}}\}$ , while the upper triangular portion contains values for the 10 targeted plastic parameters  $K = \{\hat{\theta}_{MK}\}$ . For the inverse problem, the color green denotes good conditioning, orange indicates average conditioning, and red signifies ill conditioning.

$\bigcup$	$\{\tilde{Z}\}^1$	$\{\tilde{Z}\}^2$	$\{\tilde{Z}\}^3$	$\{\tilde{Z}\}^4$	$\{\tilde{Z}\}^5$	$\{\tilde{Z}\}^6$	$\{\tilde{Z}\}^7$	$\{\tilde{Z}\}^8$	$\{\tilde{Z}\}^9$	$\{\tilde{Z}\}^{10}$	$\{\tilde{Z}\}^{11}$
$\{\tilde{Z}\}^1$		2.7	3.7	3.4	3	2.9	3.3	3.2	2.9	3.0	3.7
$\{\tilde{Z}\}^2$	1.8		2.8	2.6	2.7	2.7	3.1	2.6	2.8	(2.5)	2.7
$\{\tilde{Z}\}^3$	1.6	1.7		3.3	2.8	2.8	3.3	3.2	2.9	3.0	3.7
$\{ ilde{Z}\}^4$	1.6	1.7	1.6		2.7	2.8	3.3	3.0	2.8	2.8	3.2
$\{ ilde{Z}\}^5$	2.1	2	1.9	1.9		2.7	3.1	2.6	2.6	2.7	2.9
$\{ ilde{Z}\}^6$	1.5	1.5	1.5	1.4	1.6		3.0	2.7	2.7	2.6	2.8
$\{ ilde{Z}\}^7$	2.9	2.7	2.8	2.8	2.8	2.6		3.1	3.3	3.1	3.2
$\{ ilde{Z}\}^8$	1.4	1.6	1.2	1.2	1.7	1.4	2.7		2.7	2.7	3.2
$\{ ilde{Z}\}^9$	2.5	2.4	2.4	2.4	2.3	2.2	2.8	2.3		2.6	2.8
$\{\tilde{Z}\}^{10}$	1.5	1.7	1.4	1.4	1.8	1.4	2.7	1.2	2.4		3.1
$\{\tilde{Z}\}^{11}$	1.6	1.6	1.4	1.5	1.9	1.4	2.7	1.2	2.2	1.3	

In agreement with Renner et al. [22], all I-index values decrease when two topographies are coupled, across all three parameter sets under consideration. While only two parameter sets are reported in table 6, this trend is also observed for the parameter set limited to  $\{Q,b,\tau_0\}$  [66]. All the identifiability indices  $I_{\{h_{i,i}\in\{1,\dots,7\}}\}$  computed for the interaction coefficients are less than the critical value of 3, with most being less than 2. For the identifiability of the 10 plastic parameters, the best pair of topographies reduces the index from  $I_{\{\hat{\theta}_{MK}\}} = 2.8$  for the single topography  $\{\tilde{Z}\}^2$  to  $I_{\{\hat{\theta}_{MK}\}} = 2.5$  for the optimal combination of the topographies  $\{\tilde{Z}\}^2 \bigcup \{\tilde{Z}\}^{10}$ . This decrease indicates strong complementarity between these two topographies. Nevertheless, none of the coupling combinations results in an I-index less than 2. While the use of combined topographies improves the conditioning of the inverse problem compared to using a single topography, only moderate conditioning of the inverse problem is obtained. We

therefore investigate all possible combinations of three topographies.

While the I-index for all parameters consistently decreases when coupling of 2 topographies compared to using a single topography, this trend does not extend to the coupling of 3 topographies. In 27 of 165 combinations, the I-index increases when a third topography is added. For example,  $I_{\{\hat{\theta}_{MK}\}}\left(\{\tilde{Z}\}^1 \bigcup \{\tilde{Z}\}^2\right)$  is less than  $I_{\{\hat{\theta}_{MK}\}}\left(\{\tilde{Z}\}^1 \bigcup \{\tilde{Z}\}^2 \bigcup \{\tilde{Z}\}^3\right)$ . Additionally, it is observed that when the third topography added is either  $\{\tilde{Z}\}^7$  or  $\{\tilde{Z}\}^{11}$ , the I-index often increases. As shown in table 5, these topographies have high  $I_{\{\hat{\theta}_{MK}\}}$  values of 3.8 and 3.7, respectively.

From table 5 and table 6, the topographies with the highest  $I_{\{\hat{\theta}_{MK}\}}$  and the poorest complementarity correspond to grains 1, 3, 7 and 11, which are the closest to [101] orientation. This suggests that topographies from this region of the inverse pole figure are not suitable for identifying FCC crystal plasticity parameters. In contrast, the topographies with the lowest values of  $I_{\{\hat{\theta}_{MK}\}}$  are associated with grains 2, 6 and 9, which are located near the [100] orientation. This indicates that topographies from this region of orientations in the inverse pole figure are more appropriate for identifying FCC crystal plasticity parameters. However, combining these topographies does not further improve the conditioning of the inverse problem.

The increase in the I-index value when a third topography is added suggests that using a greater number of topography combinations provides no additional benefits in this study. Based on the analysis, the next section focuses on optimally selecting topographies to use in the FEMU process.

#### 3.4. Selection of the optimal combination of topographies

In this section, an optimal design for the FEMU process is developed based on the identifiability analysis conducted in section 3.3, using the starting point  $\{\hat{\theta}_{MK}\}$  established in section 3.2. The best *I*-index values, evaluated for single topographies as well as combinations of 2 and 3 topographies, are reported in table 7.

Table 7: Summary of the optimal a priori I-index using a single topography, and combining 2 and 3 topographies. For the inverse problem, the color green denotes good conditioning, orange indicates average conditioning, and red signifies ill conditioning.

For a single topography, the best I-index value for identifying all the targeted parameters is 2.8, achieved with the topography from grain 2. For a pair of topographies, the best I-index value is 2.5, achieved with the combination of topographies from grains 2 and 10. Finally, for triplets of topographies, the best I-index value is 2.4, achieved with the combination of topographies from grains 2, 4, and 10. The results indicate that adding a second topography reduces the I-index value by 0.3 in the best case, while adding a third topography only slightly reduces the I-index value by 0.1. However, incorporating a third topography significantly increases computational cost, adding 3 days per iteration to the FEMU process. Therefore, due to the marginal improvement in the

conditioning of the inverse problem with a third topography, we conclude that the topographies of the grains 2 and 10 represent the optimal choice for the FEMU process. The identifiability analysis enables the design of experiments, within the constraints of the database, to ensure an acceptable conditioning of the inverse problem at the starting point of the FEMU process. The following section discusses the identification of the 10 material parameters obtained through the FEMU method. This identification is performed using the optimal combination of topographies from grains 2 and 10.

# 4. Identification results

The results of the simultaneous identification of the 10 plastic parameters, based on the optimal design of experiments defined in section 3, are discussed in this section. The a priori I-index at the starting point for the optimal set of experiments obtained in section 3.4 is 2.5. This value results from combining the topographies of grains 2 and 10. While this indicates that parameter identification is feasible, the question arises whether the inverse problem sufficiently well-conditioned to ensure a unique solution starting from  $\{\theta_{MK}\}$ . The appendix V addresses this question through a numerical validation of the FEMU process using synthetic topographies, confirming the well-posed inverse problem from the starting point  $\{\hat{\theta}_{MK}\}$  using the topographies of the grains 2 and 10. The experimental topographies of grains 2 and 10 are thus used in the FEMU process. The starting point of the FEMU process,  $\{\hat{\theta}_{MK}\}$ , is summarized in table 8, along with the identified parameter values  $\{\hat{\theta}\}$  and their associated uncertainties  $\{\Delta\bar{\theta}\}\$ . The uncertainty is defined in eq. (C.5). Using the identified parameters  $\{\hat{\theta}\}$ , the topographies for all grains are simulated and presented in figs. 2 to 4 (left column).

Table 8: Starting point of the FEMU process  $\{\hat{\theta}_{MK}\}$  and the identified parameters  $\{\hat{\theta}\}$  are reported, along with the parametric uncertainty  $\{\Delta\bar{\theta}\}_i$  using eq. (C.5).

Danamatana	Q	b	$ au_0$	$h_1$	$h_2$	$h_3$	$h_4$	$h_5$	$h_6$	$h_7$
Parameters	(MPa)	(-)	(MPa)	(-)	(-)	(-)	(-)	(-)	(-)	(-)
$\{\hat{\theta}_{MK}\}$										
$\{\hat{ heta}\}$	152.20	29.40	69.13	0.21	0.46	0.69	0.28	0.15	1.05	0.10
$\{\Delta\bar{\theta}\}_i\ (\%)$	32.4	65.8	36.7	104.1	79.2	89.9	72.8	76.9	41.0	89.3

The evolution of the topographies during the FEMU process is illustrated in fig. 9. For grain 10, the pile-up initially located under the left edge of the indenter shifts and spreads along the face of the indenter tip. This pile-up aligns closely with the experimental ones. However, the two pile-ups observed on the lower right of the topography of grain 10 remain convolved even after the FEMU process. The shape of the highest pile-up also differs from the experimental one, appearing less rounded. For grain 2, the shapes of the pile-ups generally agree well with the experimental ones. The FEMU process significantly reduces the pile-up beneath the left edge of the indenter, bringing it closer to the experimental observation, albeit with a slight offset. The relative height between the pile-ups is initially inaccurate, and the FEMU process does not resolve this discrepancy, as shown in fig. 2.

The evolution of the cost function  $\omega\left(\{\theta\}\right)$  quantifies these discrepancies during the FEMU process. Its evolution, computed using the experimental topographies of grains 2 and 10, is shown in fig. 8a. Additionally, the evolution of the error  $\delta\left(\{\theta\}\right)$ , computed subsequently to the FEMU process for the indentation curves of grains 2 and 10, is reported in fig. 8a. The FEMU process converges in only 3 iterations. The cost function  $\omega\left(\{\theta\}\right)$ , based on the experimental-simulation gap between the topographies, decreases slightly from  $1.3\times10^{-4}$  to  $4.3\times10^{-5}$  in the final iteration. This decrease occurs mainly during the first iteration, after which the cost function  $\omega\left(\{\theta\}\right)$  remains nearly constant for the following two iterations. In agreement with the validations presented in appendix V and [66], the error calculated from the indentation curves also decreases, even though these data are not incorporated into the cost function.

The relative evolution of the parameters  $\{\theta\}^{(k)}$  at iteration k, compared to the starting point  $\{\hat{\theta}_{MK}\}$ , is shown in fig. 8b. Among these, the parameter b exhibits the most significant change, followed by  $h_3$ ,  $h_6$ , and  $\tau_0$ . Despite a slight decrease in the model-experiment discrepancy, fig. 8b shows a significant evolution of the parameters during the minimization process. In contrast, parameter Q evolves slightly (8%), suggesting that it could be considered fixed, thereby greatly facilitating the identification. Given its limited evolution during the identification process, the identifiability of the remaining parameters is assessed by considering Q as known. In this case, the best I-index for the remaining plastic parameters is 2.5, computed solely from the topography of grain 10. In comparison, when all ten parameters are considered, the I-index for the topography of grain 10 is 3.0, as reported in table 5. This indicates a reduction of 0.5 when Q is excluded in this case. Given the limited evolution of Q and its strong coupling with the interaction coefficients, the simultaneous identification of these parameters complicates the establishment of a well-conditioned inverse problem. The following section evaluates the validity of the identification results using the remaining topographies for validation, as well as the stability of the final solution.

#### 5. Validation

Given the parametric uncertainties reported in table 8, this section further investigates and discusses the identified parameters to validate them. It is essential to note that the parametric uncertainties computed from eq. (C.5) neglect parametric correlations. This results in an overestimation of the uncertainty values, providing an upper bound for the actual parametric uncertainties. The initial values of the parameters  $h_1$ ,  $h_2$ , and  $h_3$  fall within the limits defined by the parametric uncertainties, validating their consistency with the initial set evaluated by DDD. Nevertheless, the uncertainties remain significant, even considering the low I-index value obtained at the solution point, as illustrated in fig. 10b. The parametric uncertainties in eq. (C.5) depend on the value of the cost function  $\omega(\{\theta\})$  and the matrix  $[\bar{G}^{-1}]$ . Therefore, the experimental-simulation discrepancy leading to high parametric uncertainties can potentially be reduced by refining the constitutive model.

As a preliminary validation of the identified behavior, all topographies excluded from the FEMU process are simulated using the identified parameters  $\{\hat{\theta}\}$ . The experimental-simulation discrepancy, calculated from eq. (9) for each

topography using both the initial and identified parameter values, is illustrated in fig. 10a. Significantly, for all topographies except grain 1, the experimental-simulation gap with the  $\{\hat{\theta}\}$  set of parameters is reduced. For grain 1, the error slightly increases, with a factor close to 1. The highest reduction factor, observed for the topography of grain 9, is 3.6. For the topographies used in the FEMU process for grain 2 and 10, the reduction factors are slightly lower, at 3.2 and 2.8, respectively. The reduction factors for the gaps associated with the topographies of grains 15 and 9 are 2.6 and 2.5, respectively. For the remaining topographies, the reduction factors are below 2.

A secondary investigation of the identified parameter set focuses on the a posteriori I-index, as illustrated in fig. 10b. The I-index of all plastic parameters decreases from 2.4 to 2.1, indicating improved convexity of the cost function near the FEMU solution. This validation of the result is significant and further supports the identification results presented in this section. The I-index of the interaction coefficients, considering a known triplet  $\{Q, b, \tau_0\}$ , increases marginally from 1.8 to 1.9 when evaluated at the starting point and the optimized point, respectively. This increase is primarily attributed to the rise in the I-index value of the topography of grain 2, which increases for the interaction coefficients and the set of all targeted parameters. Overall, the FEMU process significantly enhances the complementarity of the two topographies used for identification. This results in an improved a posteriori I-index, decreasing from 2.5 prior to the FEMU process to 2.1 afterwards. These validations show that the stability of the FEMU solution is significantly improved compared to the starting point, as is the predictive capability of the model using these parameters. After validating the identification results within the same deformation regime and demonstrating improved solution stability relative to the initial starting point, the final section discusses the identified parameters.

# 6. Discussion

Table 9 presents a comparison of interaction coefficients identified in this study with a selection of interaction coefficients from the literature. All interaction coefficients  $h_{i,i\neq 1}$  and  $\alpha_{i,i\neq 1}$  are normalized by their respective self-hardening coefficients  $h_1$  and  $\alpha_1$ . This ratio normalization is essential for rigorously comparing interaction coefficients, as it eliminates dependence on their original work-hardening formulations. Since self-hardening involves dislocations moving over large areas within the grain, it is computationally expensive to evaluate with accuracy. In DDD, simulation volumes are often insufficient to reliably quantify this effect. Similarly, the present identification relies on  $20 \times 20$   $\mu m^2$  experimental topographies, which correspond to a subsurface volume that may not fully capture the self-hardening behavior. In our results, the highest parametric uncertainty pertains to the self-hardening coefficient. Nonetheless, the self-hardening coefficient identified in this study aligns closely with the value reported by Tabourot et al. [86], based on Franciosi study [27], and with the value obtained by Gérard et al. [19].

Latent hardening is initially estimated to be equal to or greater than self-hardening [27, 28, 30, 86, 87]. However, this contrasts with more recent DDD evaluations of the coefficients [33, 62, 64], which evaluate lower values for some latent hardening coefficients. The coplanar interaction coefficient  $h_2$  is often assumed to be equal to the self-hardening coefficient in table 9, as it is similarly

Table 9: Comparison of the ratios of interaction coefficients with respect to self-hardening from this study and the literature. In studies with fewer than 7 interaction coefficients,  $h_7$  is thus equal to  $h_5$  for the glissile junction (see table 3). The footnote of the table specifies the method and equations used to obtain the values: TT refers to tensile tests, CP to crystal plasticity, and DDD refers to discrete dislocation dynamics. Values of  $\alpha^{sr} = \sqrt{a^{sr}}$  are used in the case of DDD simulations and crystal plasticity models that account for the evolution of the dislocation density. As a reminder,  $h_1$  correspond to self-hardening,  $h_2$  coplanar,  $h_3$  Hirth lock,  $h_4$  collinear,  $h_5$  glissile  $G_{60^{\circ}}$ ,  $h_6$  Lomer lock, and  $h_7$  glissile  $G_{0^{\circ}}$  interaction. Sessile interactions correspond to  $(h_3, h_6)$ , and glissile ones to  $(h_1, h_2, h_4, h_5, h_7)$ .

Literature		Material	$\alpha_1$	$\frac{\alpha_2}{\alpha_1}$	$\frac{\alpha_3}{\alpha_1}$	$\frac{\alpha_4}{\alpha_1}$	$\frac{\alpha_5}{\alpha_1}$	$\frac{\alpha_6}{\alpha_1}$	$\frac{\alpha_7}{\alpha_1}$
Devincre et al.	$[35]^{1}$	Copper	0.35	1.00	0.76	2.26	1.06	1.02	1.06
Gérard et al.	$[19]^2$	Copper	0.16	0.63	1.27	23.92	4.90	4.47	4.90
Madec and Kubin	$n[62]^{1}$	Nickel	0.35	1.00	0.60	2.34	0.86	1.17	0.91
Madec et al.	[64]	Nickei	0.55	1.00	0.00	2.34	0.80	1.11	0.91
			$h_1$	$\frac{h_2}{h_1}$	$\frac{h_3}{h_1}$	$\frac{h_4}{h_1}$	$\frac{h_5}{h_1}$	$\frac{h_6}{h_1}$	$\frac{h_7}{h_1}$
Kocks	$[87]^3$		1.00	1.40	1.40	1.40	1.40	1.40	1.40
Franciosi	$[27]^3$	Copper	0.20	1.50	1.50	1.50	2.00	5.00	2.00
Tabourot et al.	[86]	Copper	0.20	1.50	1.50	1.50	2.00	5.00	2.00
Bassani and Wu	$[28]^3$	Copper	8.00	1.00	1.00	1.00	1.88	2.50	1.88
Méric et al.	$[30]^4$	Copper	1.00	4.40	4.75	4.75	4.75	5.00	4.75
Gérard et al.	$[34]^4$	Copper	1.00	1.00	0.20	90.00	3.00	2.50	3.00
Guery et al.	$[20]^4$	316LN	1.00	1.64	0.10	12.50	0.87	2.60	0.87
Present study $\{\hat{\theta}\}$	$\}^4$	Nickel	0.21	2.19	3.29	1.33	0.71	5.00	0.48
1: DDD, $\tau_c^s = \mu b \sqrt{\sum_r (\alpha^{sr})^2 \rho^r}$									
2: CP, $\dot{\gamma}^s = \dot{\gamma_0}^s \left(\frac{\tau^s}{\tau_c^s}\right)^{\frac{1}{m}}, \ \tau_c^s = q\mu b \sqrt{\sum_r (\alpha^{sr})^2 \rho^r}, \ \dot{\rho}^s = \frac{1}{bK} \left(\sqrt{\sum_r (\alpha^{sr})^2 \rho^r} - 2y_c K \rho^s\right)  \dot{\gamma}^s $									
3: TT, $h^{sr} = \frac{\tau^r}{\tau_s}$									
4: CP, $\dot{\gamma}^s = \left\langle \frac{ \tau^s  - \tau_c^s}{K} \right\rangle$	$\rangle^n$ , $\tau_c^s =$	$=  au_0 + Q \sum_r h^s$	$r_{\beta^s}, \dot{\beta}^s$	= b (1 -	$\beta^s$ ) $ \dot{\gamma}^s$	I			

difficult to evaluate through DDD simulations due to the same limitations as self-hardening. When estimating the parameters using tensile tests on single crystals, the coplanar interaction coefficient is typically slightly higher than or equal to self-hardening [27, 28]. In this study, the coplanar interaction ratio relative to self-hardening lies at the upper end of the values reported in table 9, closely aligning with those reported by Franciosi [27] and Guery et al. [20]. Notably, both the present study and the work of Guery et al. [20] initially assumed the coplanar interaction coefficient equals the self-hardening coefficient at the start of the FEMU process. However, both studies ultimately determined a slightly higher coplanar interaction coefficient, with the resulting ratios between the two coefficients comparable across the two studies.

The Hirth lock  $h_3$  is evaluated in DDD simulations as the weakest interaction [33, 35]. However, tensile tests on single crystals classify it as a strong interaction [28, 30, 87]. Initially, within the parameter set  $\{\theta_{MK}\}$ , the Hirth lock is the weakest interaction, but after the identification, it ranks as the second strongest. Its ratio to self-hardening remains within the range of values in the literature but is higher than most of the values in table 9.

Conversely, the collinear interaction  $h_4$  is evaluated in DDD simulations as the strongest interaction as reported by Madec et al. [32] and Devincre et

al. [88]. However, when estimating through tensile tests on single crystals, it does not rank as the strongest interaction, though it remains among the higher-ranked coefficients. Within the initial parameter set  $\{\hat{\theta}_{MK}\}$ ,  $h_4$  is originally the strongest interaction but ultimately ranks fourth. Its ratio to self-hardening aligns closely with the value obtained by Franciosi [27].

According to Madec et Kubin [62], the glissile interaction is split into two,  $h_5$  and  $h_7$ , while other studies in table 9 treat them as equal. When evaluated via DDD, the glissile interaction coefficients exhibit low ratios relative to self-hardening [62, 88] and rank second when estimated through tensile tests on single crystals. The  $G_{60^{\circ}}$  glissile coefficient  $h_5$  ratio to self-hardening remains close to its initial value after the FEMU process and aligns with the values identified by Guery et al. [20], while the  $G_{0^{\circ}}$  coefficient  $h_7$  exhibits a slightly lower ratio. These ratios are among the lowest in table 9.

When parameters are estimated using tensile tests on single crystals, the Lomer lock  $h_6$  is identified as the strongest interaction. In contrast, DDD evaluations rank it as a second or third strongest interaction in table 9. In this study, the Lomer lock lock's ratio relative to self-hardening aligns with values reported by Méric et al. [30] and Franciosi [27], and it is identified as the strongest interaction.

In this investigation, the coefficients  $h_6$  and  $h_3$ , corresponding to the Lomer lock and Hirth locks, respectively, are identified as the most significant interaction coefficients. These are followed by the coplanar interaction  $(h_2)$ , the collinear interaction  $(h_4)$ , initially postulated as the strongest interaction), the self-hardening  $(h_1)$ , the  $G_{60^{\circ}}$  glissile junction  $(h_5)$ , and the  $G_{0^{\circ}}$  glissile junction  $(h_7)$ . Based on the results of this study, the ranking of the interactions is as follows:

$$h_7 < h_5 < h_1 < h_4 < h_2 < h_3 < h_6.$$
 (14)

A key observation from this ranking is that lock interactions ( $h_3$  and  $h_6$ ) are identified as the strongest interactions, suggesting their dominant role over the glissile interaction.

# Conclusion

In this study, an inverse method was employed to identify crystal plasticity parameters using residual topographies obtained from nanoindentation tests. An a priori identifiability analysis was conducted to carefully select topographies, ensuring optimal conditioning by leveraging the strengths of the experimental database. Following this analysis, an optimal set of experiments was selected for the FEMU method. 10 crystal plasticity parameters were identified, leading to the following conclusions:

- (1) The identifiability analysis revealed that incorporating three topographies only slightly improved the conditioning of the inverse problem within the fixed database of eleven orientations. As a result, two topographies were used to identify the 10 crystal plasticity parameters.
- (2) In both the test and the identification process, the inverse problem successfully reduced the indentation curve error, despite not being considered in the analysis.

- (3) The parameters identified in this study significantly reduced the discrepancy between experimental and simulation results across the entire database, including topographies excluded from the FEMU process.
- (4) The stability of the solution was enhanced through the FEMU process by increasing the complementarity of the selected topographies.
- (5) The values of the interaction coefficients fell within the range reported in the literature, aligning more closely with experimentally determined values for copper than those obtained from DDD simulations for nickel.
- (6) The ranking of the interaction coefficients indicated that the sessile interactions were stronger than the glissile ones.

Finally, the identifiability analysis highlighted the importance of carefully selecting the observables to identify the targeted parameters. However, with the current experimental database, the optimal design of experiments only achieved a moderate identifiability index, indicating the potential for further improvement. To enhance the initial conditioning of the inverse problem, a key approach is to incorporate all possible crystal orientations into the a priori identifiability analysis. Additionally, Berkovich azimuth angles should be considered. Such an analysis would provide a priori guidance for designing experiments. Furthermore, a complementary approach to enhance identifiability could involve incorporating additional observables, such as lattice rotation [89], and/or residual stresses [90].

# Acknowledgement

The authors acknowledge the support of the french Agence Nationale de la Recherche (ANR), under grant ANR-22-CE08-0009 (project NOTIFICATION) and the EIPHI Graduate school (contract ANR-17-EURE-0002). We also wish to acknowledge the assistance of Mr. Thomas Helfer at CEA (French Alternative Energies and Atomic Energy Commission) for the support with the behaviour law integration using MFront software.

# ${\bf CRediT\ authorship\ contribution\ statement}$

A. Bourceret: Conceptualization, Software, Methodology, Formal analysis, Investigation, Writing – original draft, Visualization. Y. Gaillard: Conceptualization, Software, Validation, Formal analysis, Investigation, Resources, Writing – review & editing, Supervision, Funding acquisition. A. Lejeune: Conceptualization, Software, Resources, Writing – review & editing. F. Richard: Conceptualization, Methodology, Software, Validation, Formal analysis, Resources, Writing – review & editing, Supervision, Project administration, Funding acquisition.

# Declaration of competing interest

The authors declare that they have no known competing financial interests or personal relationships that could have appeared to influence the work reported in this paper.

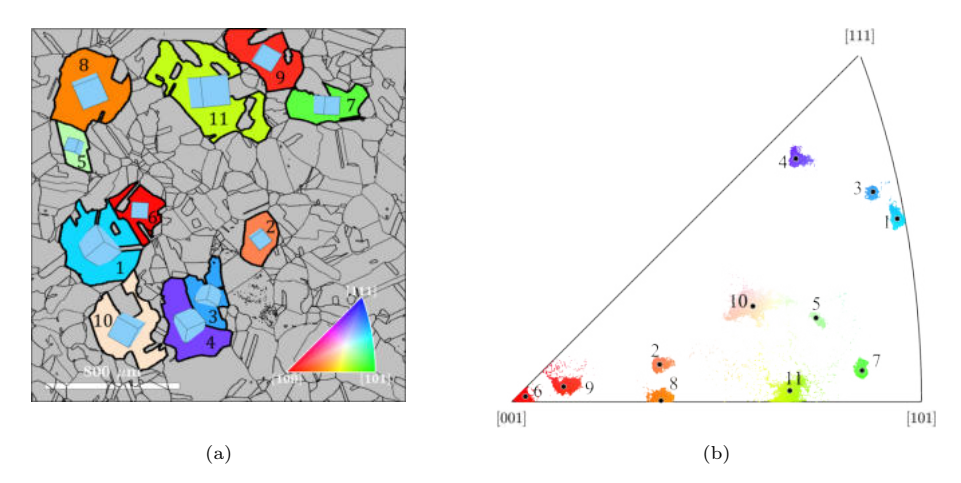


Figure 1: (a) EBSD mapping and (b) inverse pole figure of the nickel sample. In (a), the EBSD map is overlaid with oriented crystal shapes, defined by the mean orientation of each grain. In (b), the inverse pole figure displays black dots representing the mean orientation of each grain. All pixels within the selected grains are colored according to their crystallographic orientations.

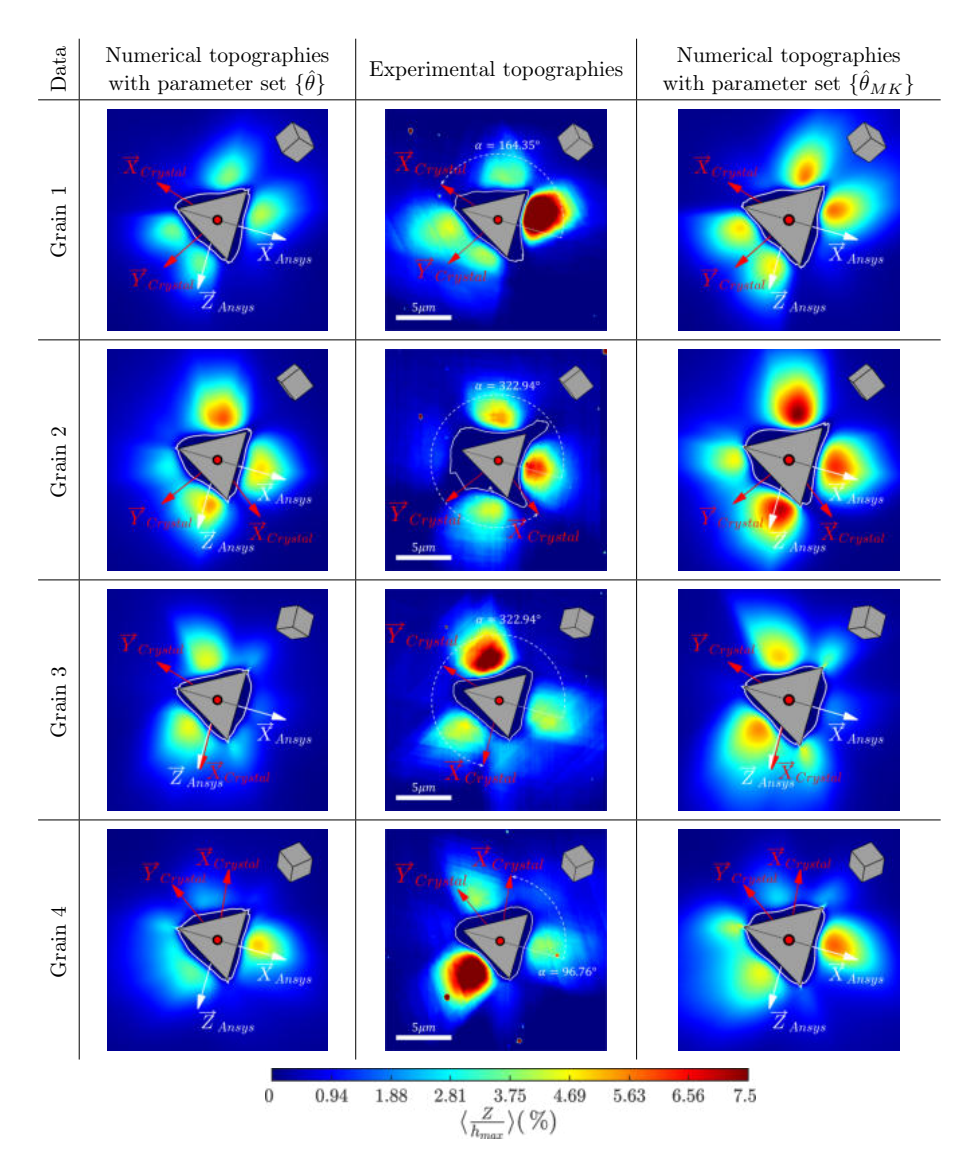


Figure 2: Representation of the experimental and numerical topographies for the grains 1 to 4. Each row corresponds to a grain, with the left column showing the topographies simulated using the identified parameters, the central column displaying the experimental topographies, and the right column showing the topography simulated using the starting point. In each topography, the indenter is depicted along with the crystal axis  $\overrightarrow{X}_{Crystal}$  and  $\overrightarrow{Y}_{Crystal}$  projected onto the indentation plane. Additionally, a white line indicates the zero level of the topography, and an oriented crystal shape corresponds to the crystallographic orientation. For the experimental topographies, azimuth angles are shown, while the reference frame orientation of the finite element model is displayed on the numerical topographies. All the topographies are squares of  $20 \times 20~\mu\text{m}^2$ , with a scale bar provided on experimental topographies.

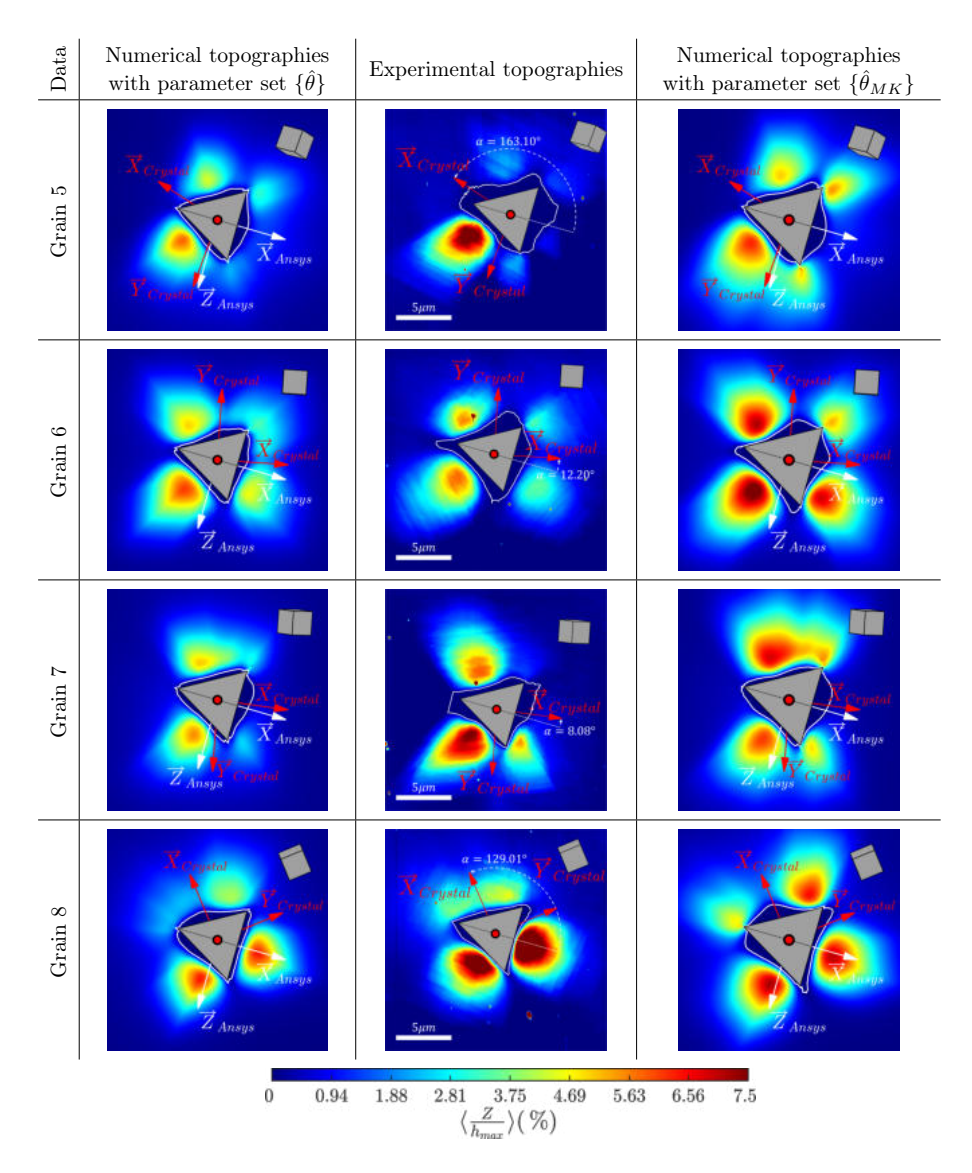


Figure 3: Representation of the experimental and numerical topographies for the grains 5 to 8. Each row corresponds to a grain, with the left column showing the topographies simulated using the identified parameters, the central column displaying the experimental topographies, and the right column showing the topography simulated using the starting point. In each topography, the indenter is depicted along with the crystal axis  $\overrightarrow{X}_{Crystal}$  and  $\overrightarrow{Y}_{Crystal}$  projected onto the indentation plane. Additionally, a white line indicates the zero level of the topography, and an oriented crystal shape corresponds to the crystallographic orientation. For the experimental topographies, azimuth angles are shown, while the reference frame orientation of the finite element model is displayed on the numerical topographies. All the topographies are squares of  $20 \times 20~\mu\text{m}^2$ , with a scale bar provided on experimental topographies.

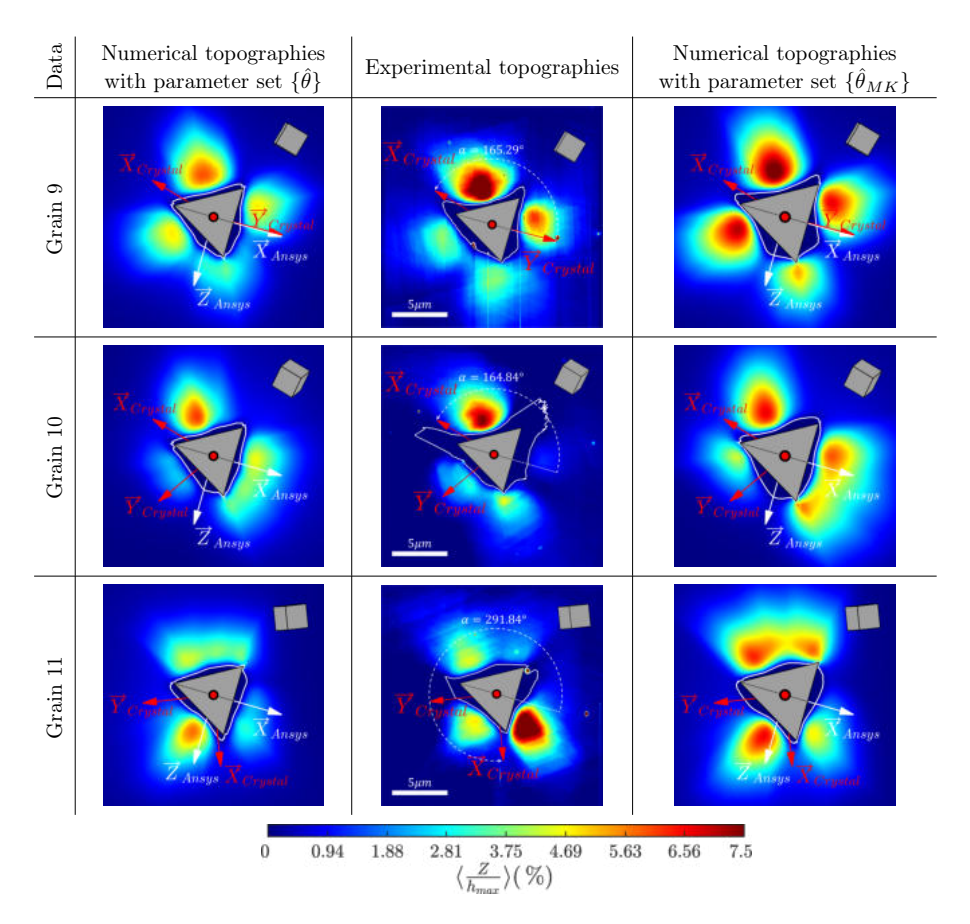


Figure 4: Representation of the experimental and numerical topographies for the grains 9 to 11. Each row corresponds to a grain, with the left column showing the topographies simulated using the identified parameters, the central column displaying the experimental topographies, and the right column showing the topography simulated using the starting point. In each topography, the indenter is depicted along with the crystal axis  $\overrightarrow{X}_{Crystal}$  and  $\overrightarrow{Y}_{Crystal}$  projected onto the indentation plane. Additionally, a white line indicates the zero level of the topography, and an oriented crystal shape corresponds to the crystallographic orientation. For the experimental topographies, azimuth angles are shown, while the reference frame orientation of the finite element model is displayed on the numerical topographies. All the topographies are squares of  $20 \times 20~\mu\text{m}^2$ , with a scale bar provided on experimental topographies.

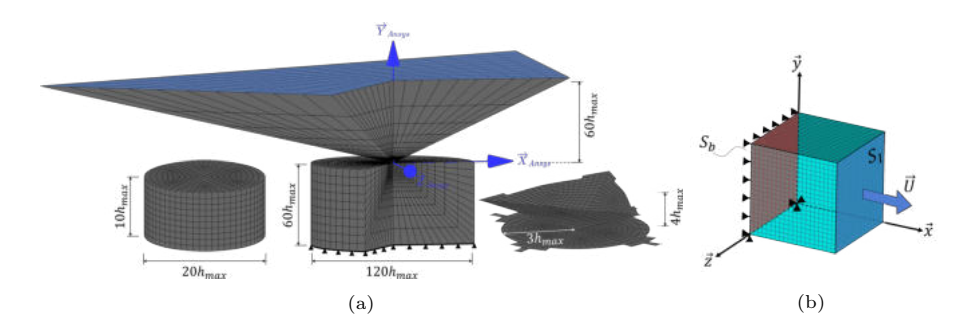


Figure 5: (a) Finite element model of the nanoindentation test. The central, finer meshed area is shown on the left, the entire mesh in the middle, and the contact area on the right. (b) The tensile test geometry. On both images, blue color on faces represent the imposed displacement face corresponding to the experiments.

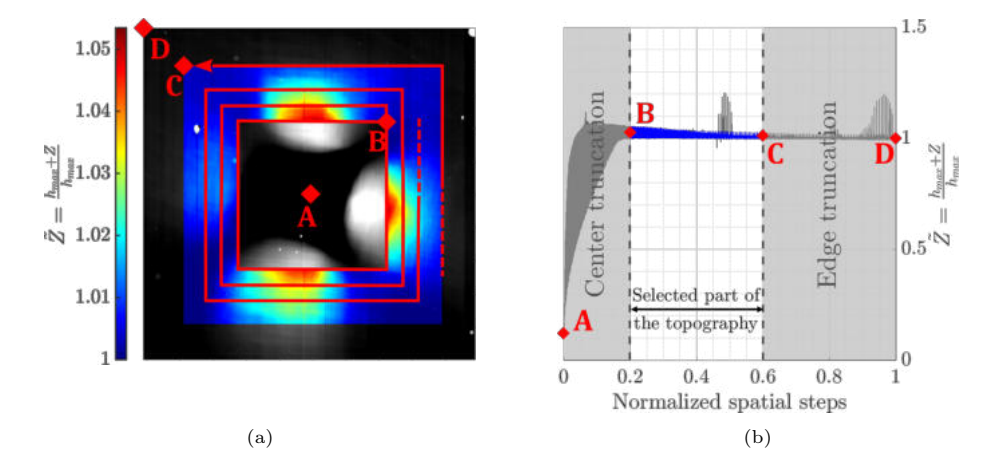


Figure 6: Data reshaping of the topographies in vectors along a path illustrated on the topography of grain 2. (a) Representation of the red path along the normalized topography  $\tilde{Z}$  from the point A to the point D. The part of the topography selected (from the point B to the point C) is colored, and the part of the topography neglected is in black and white. (b) Normalized topography  $\tilde{Z}$  as a function of the spatial steps, normalize by total number of points in the topography (512 × 512 pixels, 262144 points in total). In (b), the selected part of the topography is colored in blue.

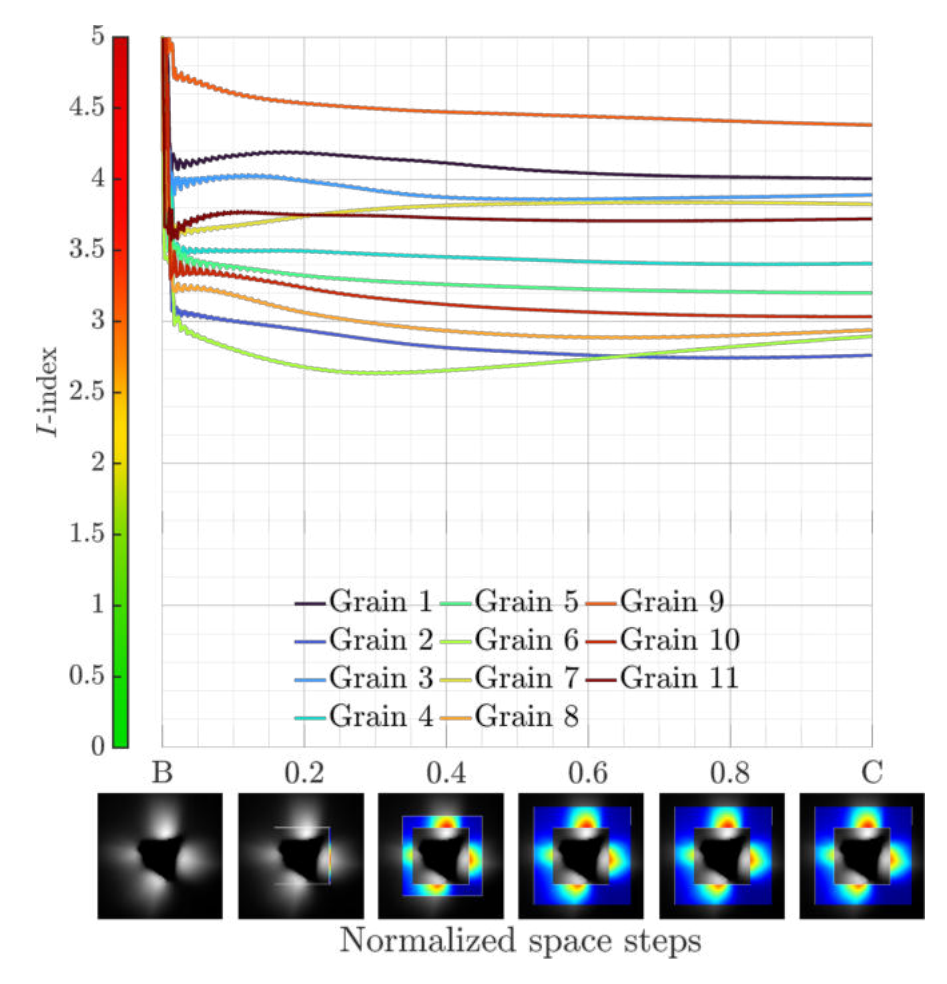


Figure 7: Evolution of the identifiability index for all the 10 targeted parameters as a function of the normalized spatial steps along the red path illustrated in fig. 6a between point B and C.

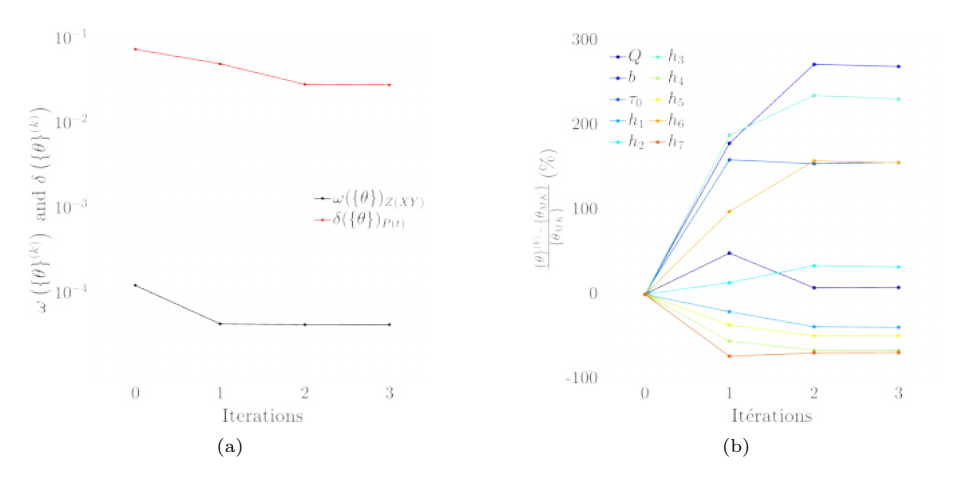


Figure 8: (a) Evolution of the cost function  $\omega\left(\{\theta\}^{(k)}\right)$  and the error on the P-h curves  $\delta\left(\{\theta\}^{(k)}\right)$  as a function of the iterations. (b) Evolution of the parameter values relative to their initial values as a function of the iterations.

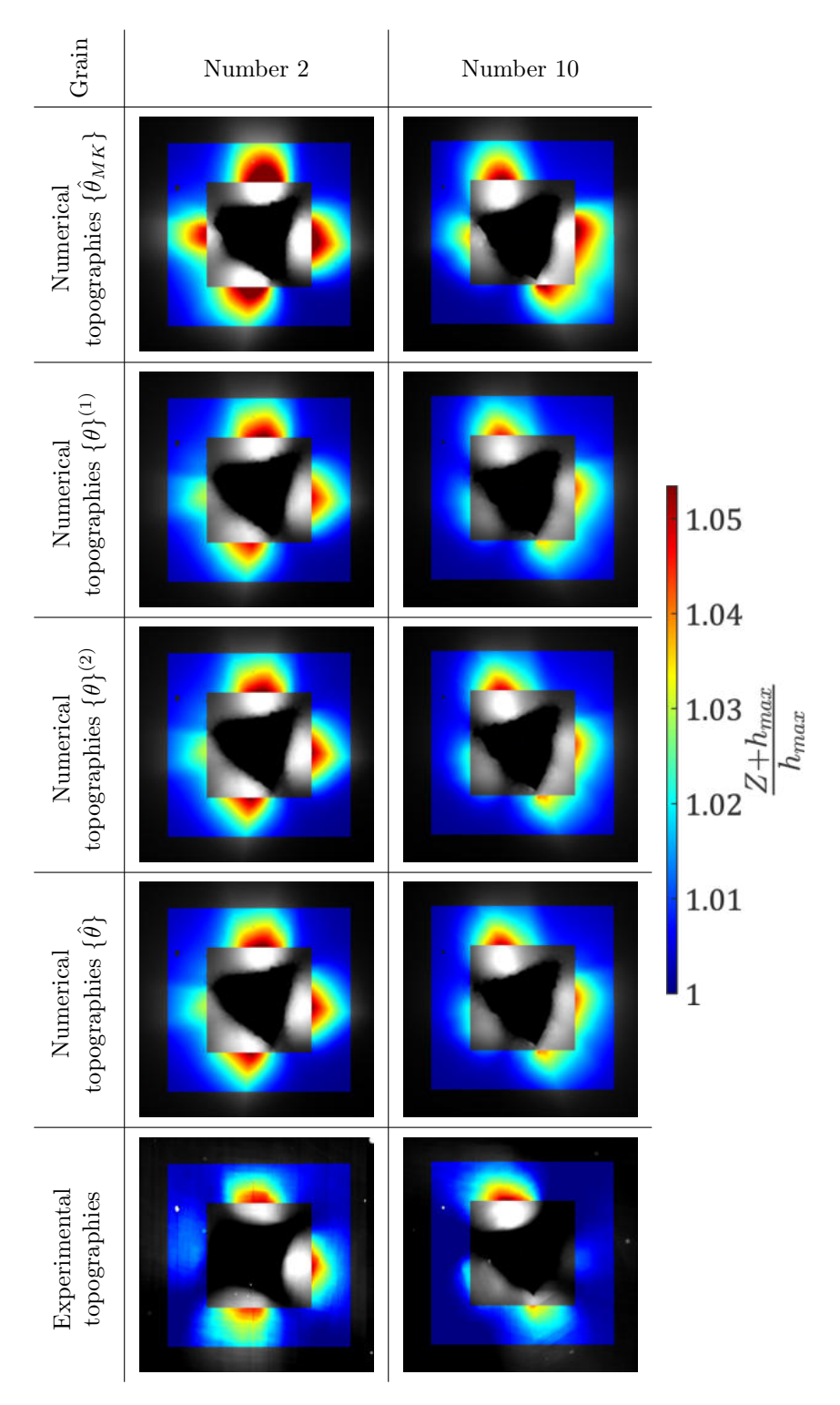
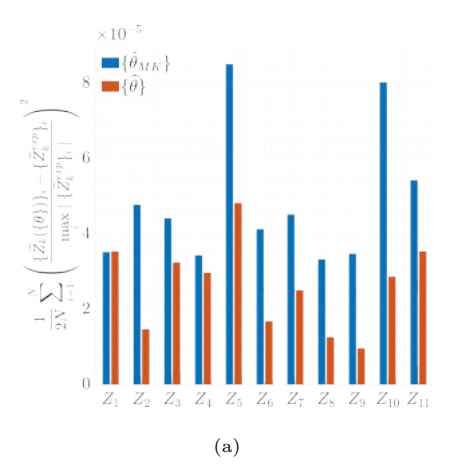


Figure 9: Evolution of the topographies across iterations. Each column represents a grain, each row corresponds to a specific iteration, and the last row shows the experimental topographies. Only the part of the topographies taken into account for the identification is colored, while the rest of the topographies is displayed in black and white.



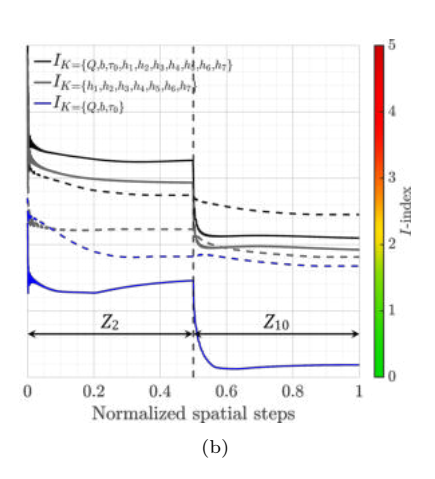
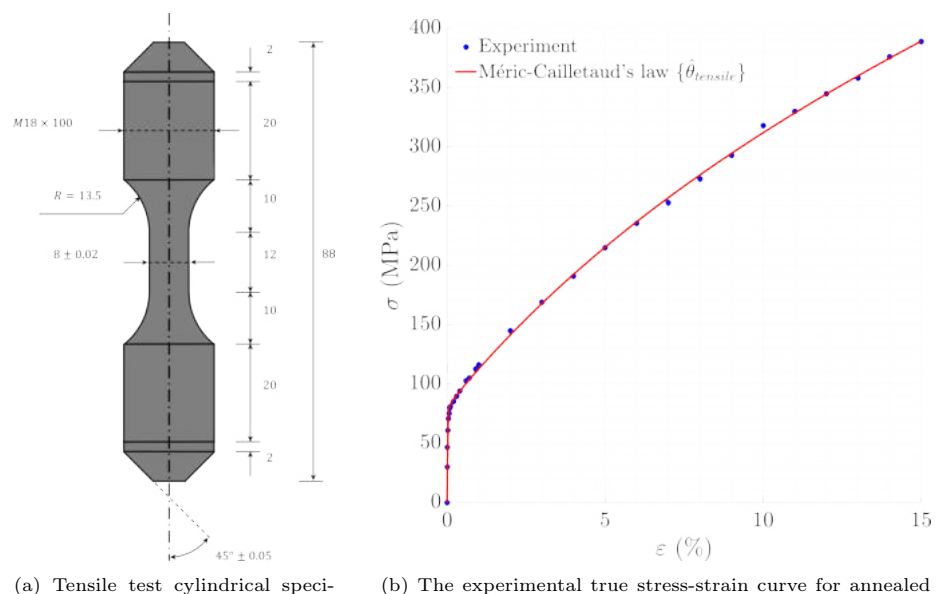


Figure 10: Identified parameters validations. (a) Deviation from experimental results across the entire topography database, using the initial parameters  $\{\hat{\theta}_{MK}\}$  and the identified parameters  $\{\hat{\theta}\}$ . (b) Comparison of the *I*-index evolution before (dashed line) and after (solid line) parameters identification.

# I. Starting point identified from tensile test curve

On a section of the polycrystalline annealed nickel sample, the longitudinal strain is measured using a strain gauge extensometer, while a constant strain rate of  $4 \times 10^{-4}$  s<sup>-1</sup> is applied. The dimension of the sample cylindrical geometry is illustrated in fig. I.1a, obtained from [52]. The true stress-true strain tensile curve of the sample, represented by blue circles, is shown in fig. I.1b. The tensile test is carried out up to 15%, revealing a very short elastic region followed by plastic flow. The simulation of the tensile test is carried out using a representative elementary volume (REV) of 1 mm<sup>3</sup> that is illustrated in fig. 5b.



- men geometry in millimeters [52]. polycr The si
- (b) The experimental true stress-strain curve for annealed polycrystalline nickel (blue circles) is obtained from [21]. The simulated tensile curve, using the identified parameter set  $\{\hat{\theta}_{MK}\}$ , is shown as a red line.

Figure I.1: Starting point identification results obtained from tensile test. The identification concerns  $\{Q, b, \tau_0\}$ , while the interaction coefficients are taken from [62]. The values of  $\{\hat{\theta}_{MK}\}$  are provided in table 4.

# II. Experimental indentation curves within grains

On a section of the sample, following surface polishing and EBSD measurements, nanoindentation tests are performed, and the corresponding indentation curves are shown in fig. II.2.

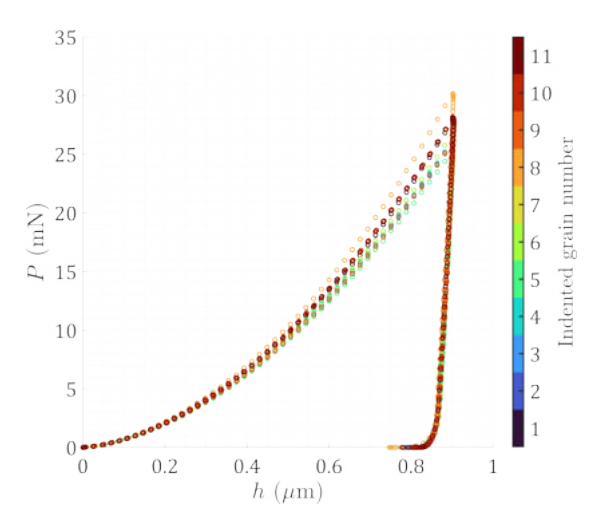


Figure II.2: Experimental indentation curves for all the selected grains are presented, with colors corresponding to the grain numbers in table 1 and fig. 1. The indentations are displacement controlled, with indentation depths reaching up to 900 nm.

Despite the heterogeneity of the crystal orientations among the selected grains fig. 1b, the indentation curves appear notably similar. A slight variation differentiates the curves, which follow consistent loading and unloading paths. These tests are analyzed in detailed in [66].

#### III. Sensitivity matrix concatenation and parametric uncertainty

The estimated parameters  $\{\hat{\theta}\}$  are obtained using the Levenberg-Marquardt algorithm [78, 79], implemented in the MIC2M software [76]. This appendix outline the assembly of sensitivity matrices for multiple topographies  $[\bar{S}]$ , the computation of the matrix  $[\bar{G}]$ , its relation to the Levenberg-Marquardt algorithm matrix  $[\underline{G}]$ , and the parametric uncertainty evaluation  $\{\Delta\bar{\theta}\,(\{\theta\})\}$ . The local sensitivity matrix  $[\bar{S}^j]$  of the j-th topography, computed for each topographies using eqs. (10) and (11), is assembled as follows:

$$[\bar{S}] = \frac{1}{M} \begin{bmatrix} \bar{S}_{1,1}^{1} & \dots & \bar{S}_{1,j}^{1} & \dots & \bar{S}_{1,N_{\theta}}^{1} \\ \vdots & & \vdots & & \vdots \\ \bar{S}_{N_{1},1}^{1} & \dots & \bar{S}_{N_{1},j}^{1} & \dots & \bar{S}_{N_{1},N_{\theta}}^{1} \\ \bar{S}_{N_{1}+1,1}^{2} & \dots & \bar{S}_{N_{1}+1,j}^{2} & \dots & \bar{S}_{N_{1}+1,N_{\theta}}^{2} \\ \vdots & & \vdots & & \vdots \\ \bar{S}_{N_{1}+1,1}^{M-1} & \dots & \bar{S}_{N_{1}+1,j}^{M-1} & \dots & \bar{S}_{N_{1}+1,N_{\theta}}^{M-1} \\ \vdots & & \vdots & & \vdots \\ \bar{S}_{(\sum_{o=1}^{M-1} N_{o}),1}^{M-1} & \dots & \bar{S}_{(\sum_{o=1}^{M-1} N_{o}),j}^{M-1} & \dots & \bar{S}_{(\sum_{o=1}^{M-1} N_{o})+1,N_{\theta}}^{M-1} \\ \vdots & & \vdots & & \vdots \\ \bar{S}_{N_{1}+1,1}^{M-1} & \dots & \bar{S}_{(\sum_{o=1}^{M-1} N_{o}),j}^{M-1} & \dots & \bar{S}_{(\sum_{o=1}^{M} N_{o}),N_{\theta}}^{M-1} \end{bmatrix} .$$
 (C.1)

The evaluation of the sensitivity matrix is incorporated into the identifiability analysis through the matrix  $[\bar{G}]$ , defined as follows:

$$\left[\bar{G}\right] = \left[\bar{S}\right]^T \left[\bar{S}\right]. \tag{C.2}$$

Similarly, the estimates of the parameters at each iteration are calculated using [79]:

$$\{\theta\}^{(k+1)} = \{\theta\}^{(k)} - \left( [\underline{G}]^{(k)} + \lambda^{(k)} [I] \right)^{-1} \cdot \{g\}^{(k)}$$
 (C.3)

In this equation,  $[\underline{G}]$  corresponds to an approximation of the hessian of the cost function  $\omega(\{\theta\})$ , as expressed in eq. (9), and  $\{g\}$  represents its gradient. The parameter  $\lambda^k$  perturbs the quasi-hessian matrix  $[\underline{G}]$ , being large far from the solution and diminishing as the parameters approach the solution. A relationship between the matrices, used for the calculation of the identifiability index eq. (C.2), and the approximated hessian used eq. (C.3), is expressed as follows (no summation):

$$\bar{G}_{ij} = \theta_i \theta_j \sqrt{G_{ii} G_{jj}} \underline{G}_{ij}. \tag{C.4}$$

From the computation of the cost function  $\omega\{\theta\}$  and the evaluation of the matrix  $[\bar{G}]$ , the parametric uncertainty can be expressed as a rectangular :

$$\{\Delta \bar{\theta} \left(\{\theta\}\right)\}_i = \sqrt{\frac{2\omega \left(\{\theta\}\right) \left[\bar{G}^{-1}\right]_{ii}}{M}} \tag{C.5}$$

Graphical representations and details regarding the parametric uncertainty  $\{\Delta \bar{\theta}\}_i$  are available in literature [66, 71, 76].

## IV. I-index with combinations of three topographies

In the tables IV.1 and IV.2, the identifiability index for combinations of three topographies from the entire database is presented.

Table IV.1: The identifiability index for all targeted parameters using combinations of three topographies. Indices are computed for all possible topography triplets in the experimental database, with the lowest identifiability index for the full set of 10 parameters circled in blue. Combinations are organized in the table such that the first column lists the first topography of the combination, the first row lists the second topography, and the second column lists the third topography. For the inverse problem, the color green denotes good conditioning, orange indicates average conditioning, and red signifies ill conditioning.

	U	$\{\tilde{Z}\}^2$	$2\{ ilde{Z}\}^3$	$\{ ilde{Z}\}$	$^4\{ ilde{Z}\}^5$	$\tilde{S}\{ ilde{Z}\}^{6}$	$^{6}\{ ilde{Z}\}^{7}$	$^{7}\{ ilde{Z}\}^{8}$	$\{ ilde{Z}\}^{5}$	$9\{\tilde{Z}\}^{10}$
$\{ ilde{Z}\}^1$	$\{ ilde{Z}\}^3$	2.8*								
	$\{\tilde{Z}\}^4$	2.6	3.4							
	$\begin{split} &\{\tilde{Z}\}^{3} \\ &\{\tilde{Z}\}^{4} \\ &\{\tilde{Z}\}^{5} \\ &\{\tilde{Z}\}^{6} \\ &\{\tilde{Z}\}^{7} \\ &\{\tilde{Z}\}^{8} \\ &\{\tilde{Z}\}^{9} \end{split}$	2.7	2.8	2.8						
	$\{ ilde{Z}\}^6$	2.6	2.9	2.9	2.7					
	$\{\tilde{Z}\}^7$	2.9*	3.1	3.0	3.0	2.9				
	$\{ ilde{Z}\}^8$	2.6	3.3	3.1	2.7	2.8	2.9			
	$\{ ilde{Z}\}^9$	2.7	2.9	2.8	2.6	2.7	3.1	2.6		
	$\{\tilde{Z}\}^{10}$	2.6	3.0	2.9	2.7	2.7	2.9	2.8	2.6	
	$\{\tilde{Z}\}^{11}$	2.7	3.7	3.3	2.9	2.9	3.0	3.3*	2.8	3.1*
	$\{\tilde{Z}\}^4$		2.7							
	$\{ ilde{Z}\}^5$		2.6	2.5						
	$\{ ilde{Z}\}^6$		2.6	2.5	2.5					
$\{\tilde{Z}\}^2$	$\begin{array}{l} \{\tilde{Z}\}^4 \\ \{\tilde{Z}\}^5 \\ \{\tilde{Z}\}^6 \\ \{\tilde{Z}\}^7 \\ \{\tilde{Z}\}^8 \\ \{\tilde{Z}\}^9 \end{array}$		2.9*	2.9*	2.9*	2.7*				
(2)	$\{ ilde{Z}\}^8$		2.5	2.4	2.4	2.6	2.8			
	$\{ ilde{Z}\}^9$		2.7	2.6*	2.6	2.6	2.7	2.6		
	$\{ ilde{Z}\}^{10}$		2.5	2.4	2.5	2.5	2.9	2.5	2.5	
	$\{ ilde{Z}\}^{11}$		2.7	2.6	2.6	2.6	2.8	2.6	2.6	2.6
$\{ ilde{Z}\}^3$	$\{\tilde{Z}\}^{5}$ $\{\tilde{Z}\}^{6}$ $\{\tilde{Z}\}^{7}$ $\{\tilde{Z}\}^{8}$ $\{\tilde{Z}\}^{9}$ $\{\tilde{Z}\}^{10}$			2.7						
	$\{ ilde{Z}\}^6$			2.9	2.6					
	$\{\tilde{Z}\}^7$			3.1	3.0*	2.8*				
	$ \tilde{Z} ^8$			3.1	2.6	2.7	2.8			
	$ \tilde{\{} ilde{Z} ilde{\}}^9 $			2.8	2.5	2.7	3.1	2.7		
	$\{\tilde{Z}\}^{10}$			2.9	2.7	2.6	2.9	2.8	2.6	
	$\{\tilde{Z}\}^{11}$			3.3	2.8	2.9*	3.0	3.3*	2.8	3.1*

 $<sup>^*</sup>$  highlight an increase of the I-index by adding a third topography.

Table IV.2: The identifiability index for all targeted parameters using combinations of three topographies. Indices are computed for all possible topography triplets in the experimental database, with the lowest identifiability index for the full set of 10 parameters circled in blue. Combinations are organized in the table such that the first column lists the first topography of the combination, the first row lists the second topography, and the second column lists the third topography. For the inverse problem, the color green denotes good conditioning, orange indicates average conditioning, and red signifies ill conditioning.

	U	$\{\tilde{Z}\}^5\{\tilde{Z}\}^6\{\tilde{Z}\}$	${}^{7}\{\tilde{Z}\}^{8}\{\tilde{Z}\}^{9}\{\tilde{Z}\}^{10}$
$\{ ilde{Z}\}^4$	$\{ ilde{Z}\}^6 \ \{ ilde{Z}\}^7$	2.6 2.9 *2.8	
	$\{\tilde{Z}\}^8$ $\{\tilde{Z}\}^9$	2.6       2.7       2.8         2.5       2.6       3.0	2.6
	$\begin{array}{c} \{\tilde{Z}\}^{10} \\ \{\tilde{Z}\}^{11} \end{array}$	2.6 2.6 2.9 2.7 *2.8 *3.0	2.7 2.5 3.1 *2.7 2.9 *
	$\{ ilde{Z}\}^7 \mid \{ ilde{Z}\}^8 \mid$	2.7 $2.6$ $2.7$	
$\{\tilde{Z}\}^5$	$\{\tilde{Z}\}^9$	2.6 2.9	2.5
	$\begin{array}{c} \{\tilde{Z}\}^{10} \\ \{\tilde{Z}\}^{11} \end{array}$		2.6 2.5 2.7 *2.6 *2.8 *
	$\{\tilde{Z}\}^8$	2.8	2.1 2.0 2.8
$\{ ilde{Z}\}^6$	$\{ ilde{Z}\}^9$	2.9	2.6
	$\{\tilde{Z}\}^{10} \ \{\tilde{Z}\}^{11}$	2.7	2.5 2.5 2.7 *2.7 *2.6 *
$\{ ilde{Z}\}^7$	$\{ ilde{Z}\}^9 \ \{ ilde{Z}\}^{10}$		2.9 2.8 2.9
	$\{\tilde{Z}\}^{11}$		2.8 2.8 2.8
$\{\tilde{Z}\}^8$	$\{\tilde{Z}\}^{10} \ \{\tilde{Z}\}^{11}$		2.5 2.7 2.8 *
$-\frac{1}{\{\tilde{Z}\}^9}$	$\{\tilde{Z}\}^{11}$		2.6

<sup>\*</sup> highlight an increase of the I-index by adding a third topography.

## V. Numerical validation test

A numerical validation test is conducted, it aims to recover a known solution for the 10 parameters through the FEMU process. A pseudo-experimental dataset of simulated topographies for grains 2 and 10 is generated using the starting point  $\{\hat{\theta}_{INI}\}$ . This dataset is obtained by perturbing  $\{\hat{\theta}_{MK}\}$  by  $\pm 20\%$ , and the parameter values are listed in table V.3. This perturbation magnitude is commonly used to validate FEMU processes [20, 48, 74].

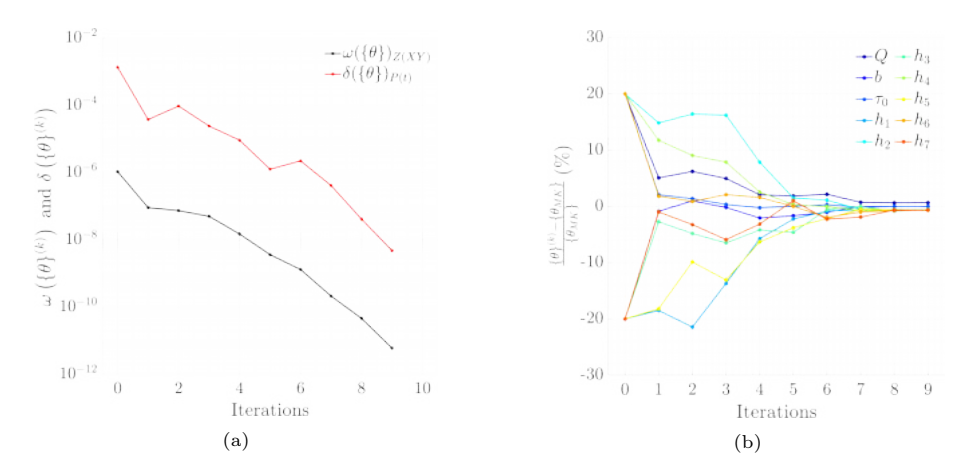


Figure V.3: (a) Evolution of the cost function  $\omega\left(\{\theta\}^{(k)}\right)$  and the error on the P-h curves  $\delta\left(\{\theta\}^{(k)}\right)$  as a function of the iterations. (b) Evolution of the relative error on the evaluation of the parameters as a function of the iteration.

Using the optimal experimental design obtained in section 3, the FEMU process required 250 finite element calculations and took 1.5 months to complete. The evolutions of the cost function and the parameters are illustrated in the fig. V.3. The estimated parameters  $\{\hat{\theta}_{test}\}$  are reported in table V.3, along with the relative error  $e_r$ .

Table V.3: Numerical validation test results. The starting point  $\{\theta_{INI}\}$  is generated by applying a  $\pm$  20% perturbation to the reference parameter set  $\{\hat{\theta}_{MK}\}$ , listed in table 4. The identified parameters  $\{\hat{\theta}_{test}\}$  and their relative error  $e_r = \frac{\{\hat{\theta}_{test}\} - \{\hat{\theta}_{MK}\}}{\{\hat{\theta}_{MK}\}}$  are reported.

Parameters	Q (MPa)	$b \\ (-)$	$ au_0  ag{MPa}$	$h_1$ $(-)$	$h_2$ $(-)$	$h_3$ $(-)$	$h_4$ $(-)$	$h_5$ $(-)$	$h_6$ $(-)$	$h_7$ $(-)$
	140.65									
$\{ heta_{INI}\}$	168.78	6.37	32.40	0.28	0.42	0.17	0.98	0.24	0.49	0.26
$\{\hat{\theta}_{test}\}$	141.58	7.96	27.00	0.35	0.35	0.21	0.82	0.30	0.41	0.32
$e_r$ (%)	0.66	-0.03	-0.01	-0.58	-0.59	-0.61	-0.59	-0.65	-0.70	-0.68

The cost function  $\omega(\{\theta\})$ , computed using eqs. (9) and (10), decreases from  $1.1 \times 10^{-6}$  to  $6.1 \times 10^{-12}$  during the minimization, as illustrated in fig. V.3a. This numerical validation test demonstrates a reduction in the gap between the perturbed and reference observables by six orders of magnitude. Additionally, fig. V.3a shows the error  $\delta(\{\theta\})$  calculated for the indentation curves. A de-

crease in  $\delta(\{\theta\})$  is observed during the optimization process, even through it is not included in the cost function.

The evolution of the parameters during the FEMU process is shown in fig. V.3b. The parameters b and  $\tau_0$  are rapidly identified by the third iteration, undergoing only minor adjustments thereafter until the FEMU process concludes. Parameter Q stabilizes by the fourth iteration, and the interaction coefficients stabilize two iterations later. By the eighth iteration, all parameters reach a stable state. As shown in table V.3 and fig. V.3b, the computed error  $e_r$  is nearly zero for b and  $\tau_0$ , indicating that their identification is more straightforward compared to the other parameters.

The relative error in table V.3 is slightly larger for the parameter Q and the interaction coefficients, despite their absolute values being nearly equal. Similar results were observed in another test case [66]. The parameter Q is estimated with a relative error of +0.66%, while the interaction coefficients exhibit a mean error of -0.62%. The interaction coefficients appear to offset one other with respect to Q. One possible explanation is related to strain hardening saturation, which can be expressed using eq. (7) for infinite slip on each slip system, as follows:

$$\lim_{\gamma^r \to \infty} R^s = Q \sum_r h^{sr}.$$
 (E.1)

When strain hardening reaches saturation, it converges to a scalar value that can be balanced across slip system through the interaction coefficients and the parameter Q. Finally, all parameters exhibit errors of less than 1%, which validate the FEMU process along with the observables selected in the section 3.

## References

- [1] A. Aburakhia, A. Bonakdar, M. Molavi-Zarandi, J. Kelleher, H. Abdolvand, Deformation mechanisms of additively manufactured Hastelloy-X: A neutron diffraction experiment and crystal plasticity finite element modeling, Materials & Design 222 (2022) 111030. URL: https://www.sciencedirect.com/science/article/pii/S0264127522006529. doi:10.1016/j.matdes.2022.111030.
- [2] V. Prithivirajan, P. Ravi, D. Naragani, M. D. Sangid, Direct comparison of microstructure-sensitive fatigue crack initiation via crystal plasticity simulations and in situ high-energy X-ray experiments, Materials & Design 197 (2021) 109216. URL: https://www.sciencedirect.com/science/ article/pii/S0264127520307516. doi:10.1016/j.matdes.2020.109216.
- [3] S. Breumier, A. Villani, C. Maurice, M. Lévesque, G. Kermouche, Effect of crystal orientation on indentation-induced residual stress field: Simulation and experimental validation, Materials & Design 169 (2019) 107659. URL: https://www.sciencedirect.com/science/article/pii/S0264127519300966. doi:10.1016/j.matdes.2019.107659.
- [4] S. Breumier, S. Sao-Joao, A. Villani, M. Lévesque, G. Kermouche, High strain rate micro-compression for crystal plasticity constitutive law parameters identification, Materials & Design 193 (2020) 108789. URL: https://www.sciencedirect.com/science/article/pii/ S0264127520303233. doi:10.1016/j.matdes.2020.108789.
- [5] M. Yaghoobi, S. Ganesan, S. Sundar, A. Lakshmanan, S. Rudraraju, J. E. Allison, V. Sundararaghavan, PRISMS-Plasticity: An opensource crystal plasticity finite element software, Computational Materials Science 169 (2019) 109078. URL: https://www.sciencedirect.com/ science/article/pii/S0927025619303696. doi:10.1016/j.commatsci. 2019.109078.
- [6] Ansys, Ansys 2022 R1 (2022). URL: https://www.ansys.com/fr-fr.
- [7] R. Quey, M. Kasemer, The Neper/FEPX Project: Free / Open-source Polycrystal Generation, Deformation Simulation, and Post-processing, IOP Conference Series: Materials Science and Engineering 1249 (2022) 012021. URL: https://dx.doi.org/10.1088/1757-899X/1249/1/012021, publisher: IOP Publishing.
- [8] G. Cailletaud, K. Sai, L. Taleb, Multi-mechanism modeling of inelastic material behavior, ISTE-Wiley, 2018. URL: https://hal-mines-paristech.archives-ouvertes.fr/hal-01706989. doi:10.1002/9781118845103.
- [9] F. Roters, M. Diehl, P. Shanthraj, P. Eisenlohr, C. Reuber, S. Wong, T. Maiti, A. Ebrahimi, T. Hochrainer, H.-O. Fabritius, S. Nikolov, M. Friák, N. Fujita, N. Grilli, K. Janssens, N. Jia, P. Kok, D. Ma, F. Meier, E. Werner, M. Stricker, D. Weygand, D. Raabe, DAMASK The Düsseldorf Advanced Material Simulation Kit for modeling multi-physics crystal plasticity, thermal, and damage phenomena from the single crystal up to the component scale. Computational Materials Science 158

- (2019) 420-478. URL: https://linkinghub.elsevier.com/retrieve/pii/S0927025618302714. doi:10.1016/j.commatsci.2018.04.030.
- [10] T. Helfer, B. Michel, J.-M. Proix, M. Salvo, J. Sercombe, M. Casella, Introducing the open-source mfront code generator: Application to mechanical behaviours and material knowledge management within the PLEIADES fuel element modelling platform, Computers & Mathematics with Applications 70 (2015) 994–1023. URL: https://www.sciencedirect.com/science/article/pii/S0898122115003132. doi:10.1016/j.camwa.2015.06.027, number: 5.
- [11] S. El Shawish, L. Cizelj, Combining Single- and Poly-Crystalline Measurements for Identification of Crystal Plasticity Parameters: Application to Austenitic Stainless Steel, Crystals 7 (2017) 181. URL: https://www.mdpi.com/2073-4352/7/6/181. doi:10.3390/cryst7060181, number: 6 Publisher: Multidisciplinary Digital Publishing Institute.
- [12] K. Sedighiani, M. Diehl, K. Traka, F. Roters, J. Sietsma, D. Raabe, An efficient and robust approach to determine material parameters of crystal plasticity constitutive laws from macro-scale stress-strain curves, International Journal of Plasticity 134 (2020) 102779. URL: https://www.sciencedirect.com/science/article/pii/S0749641919308769. doi:10.1016/j.ijplas.2020.102779.
- [13] D. J. Savage, Z. Feng, M. Knezevic, Identification of crystal plasticity model parameters by multi-objective optimization integrating microstructural evolution and mechanical data, Computer Methods in Applied Mechanics and Engineering 379 (2021) 113747. URL: https://www.sciencedirect.com/science/article/pii/S0045782521000839. doi:10.1016/j.cma.2021.113747.
- [14] B. Yin, X. Xue, B. Tang, W. Y. Wang, H. Kou, J. Li, Experiments and crystal plasticity simulations for the deformation behavior of nanoindentation: Application to the 2 phase of TiAl alloy, Materials Science and Engineering: A 831 (2022) 142283. URL: https://linkinghub.elsevier.com/retrieve/pii/S0921509321015471. doi:10.1016/j.msea.2021.142283.
- [15] K. Veasna, Z. Feng, Q. Zhang, M. Knezevic, Machine learning-based multi-objective optimization for efficient identification of crystal plasticity model parameters, Computer Methods in Applied Mechanics and Engineering 403 (2023) 115740. URL: https://www.sciencedirect.com/science/ article/pii/S0045782522006958. doi:10.1016/j.cma.2022.115740.
- [16] J. K. Engels, N. Vajragupta, A. Hartmaier, Parameterization of a Non-local Crystal Plasticity Model for Tempered Lath Martensite Using Nanoindentation and Inverse Method, Frontiers in Materials 6 (2019). URL: https://www.frontiersin.org/journals/materials/ articles/10.3389/fmats.2019.00247/full. doi:10.3389/fmats.2019. 00247, publisher: Frontiers.
- [17] P. T. N. Nguyen, F. Abbès, J.-S. Lecomte, C. Schuman, B. Abbès, Inverse Identification of Single-Crystal Plasticity Parameters of HCP Zinc from Nanoindentation Curves and Residual Topographies, Nanomaterials 12

- (2022) 300. URL: https://www.mdpi.com/2079-4991/12/3/300. doi:10.3390/nano12030300, number: 3.
- [18] K. Frydrych, Modelling Irradiation Effects in Metallic Materials Using the Crystal Plasticity Theory—A Review, Crystals 13 (2023) 771. URL: https://www.mdpi.com/2073-4352/13/5/771. doi:10.3390/cryst13050771, number: 5.
- [19] C. Gérard, G. Cailletaud, B. Bacroix, Modeling of latent hardening produced by complex loading paths in FCC alloys, International Journal of Plasticity 42 (2013) 194-212. URL: https://linkinghub.elsevier.com/retrieve/pii/S0749641912001635. doi:10.1016/j.ijplas.2012.10.010.
- [20] A. Guery, F. Hild, F. Latourte, S. Roux, Identification of crystal plasticity parameters using DIC measurements and weighted FEMU, Mechanics of Materials 100 (2016) 55-71. URL: https://www.sciencedirect.com/science/article/pii/S0167663616300813. doi:10.1016/j.mechmat.2016.06.007.
- [21] E. Renner, Y. Gaillard, F. Richard, F. Amiot, P. Delobelle, Sensitivity of the residual topography to single crystal plasticity parameters in Berkovich nanoindentation on FCC nickel, International Journal of Plasticity 77 (2016) 118-140. URL: https://linkinghub.elsevier.com/retrieve/pii/S0749641915001680. doi:10.1016/j.ijplas.2015.10.002.
- [22] E. Renner, A. Bourceret, Y. Gaillard, F. Amiot, P. Delobelle, F. Richard, Identifiability of single crystal plasticity parameters from residual topographies in Berkovich nanoindentation on FCC nickel, Journal of the Mechanics and Physics of Solids 138 (2020). doi:10.1016/j.jmps.2020.103916.
- [23] K. Goto, I. Watanabe, T. Ohmura, Inverse estimation approach for elastoplastic properties using the load-displacement curve and pile-up topography of a single Berkovich indentation, Materials & Design 194 (2020) 108925. URL: https://www.sciencedirect.com/science/article/pii/ S0264127520304597. doi:10.1016/j.matdes.2020.108925.
- [24] M. Wang, J. Wu, X. Zhan, R. Guo, Y. Hui, H. Fan, On the determination of the anisotropic plasticity of metal materials by using instrumented indentation, Materials & Design 111 (2016) 98-107. URL: https://www.sciencedirect.com/science/article/pii/S0264127516311388. doi:10.1016/j.matdes.2016.08.076.
- [25] G. I. Taylor, Plastic strain in metals, Journal of the Institute of Metals 62 (1938) 307–324.
- [26] P. Franciosi, M. Berveiller, A. Zaoui, Latent hardening in copper and aluminium single crystals, Acta Metallurgica 28 (1980) 273-283. URL: https://linkinghub.elsevier.com/retrieve/ pii/0001616080901625. doi:10.1016/0001-6160(80)90162-5.
- [27] P. Franciosi, in: Proc. Int. Symp. Metallurgy and Material Science, Risø, Denmark, 1987, p. 83.

- [28] J. L. Bassani, T.-y. Wu, Latent hardening in single crystals. II. Analytical characterization and predictions, Proceedings of the Royal Society of London. Series A: Mathematical and Physical Sciences 435 (1991) 21–41. URL: https://royalsocietypublishing.org/doi/10.1098/rspa.1991.0128. doi:10.1098/rspa.1991.0128.
- [29] T.-Y. Wu, J. L. Bassani, C. Laird, Latent hardening in single crystals I. Theory and experiments, Proceedings of the Royal Society of London. Series A: Mathematical and Physical Sciences 435 (1991) 1–19. URL: https://royalsocietypublishing.org/doi/10.1098/rspa.1991.0127. doi:10.1098/rspa.1991.0127.
- [30] L. Méric, G. Cailletaud, M. Gaspérini, F.E. calculations of copper bicrystal specimens submitted to tension-compression tests, Acta Metallurgica et Materialia 42 (1994) 921–935. URL: https://linkinghub.elsevier.com/retrieve/pii/0956715194902879. doi:10.1016/0956-7151(94)90287-9.
- [31] K. S. Havner, Further investigation of crystal hardening inequalities in (110) channel die compression, Proceedings of the Royal Society A: Mathematical, Physical and Engineering Sciences 464 (2008) 1955– 1982. URL: https://royalsocietypublishing.org/doi/10.1098/rspa. 2007.0272. doi:10.1098/rspa.2007.0272, number: 2096 Publisher: Royal Society.
- [32] R. Madec, B. Devincre, L. Kubin, T. Hoc, D. Rodney, The Role of Collinear Interaction in Dislocation-Induced Hardening, Science 301 (2003) 1879– 1882. URL: https://www.science.org/doi/10.1126/science.1085477. doi:10.1126/science.1085477, number: 5641.
- [33] L. Kubin, B. Devincre, T. Hoc, Modeling dislocation storage rates and mean free paths in face-centered cubic crystals, Acta Materialia 56 (2008) 6040-6049. URL: https://linkinghub.elsevier.com/retrieve/pii/S1359645408005788. doi:10.1016/j.actamat.2008.08.012.
- [34] C. Gérard, B. Bacroix, M. Bornert, G. Cailletaud, J. Crépin, S. Leclercq, Hardening description for FCC materials under complex loading paths, Computational Materials Science 45 (2009) 751-755. URL: https:// linkinghub.elsevier.com/retrieve/pii/S0927025608003960. doi:10. 1016/j.commatsci.2008.08.027, number: 3.
- [35] B. Devincre, L. Kubin, T. Hoc, Physical analyses of crystal plasticity by DD simulations, Scripta Materialia 54 (2006) 741-746. URL: https:// linkinghub.elsevier.com/retrieve/pii/S1359646205007128. doi:10. 1016/j.scriptamat.2005.10.066, number: 5.
- [36] Y. Guilhem, Étude numérique des champs mécaniques locaux dans les agrégats polycristallins d'acier 316L sous chargement de fatigue, Thèse, Ecole national supérieur de Paris, 2012. URL: https://pastel.hal.science/pastel-00732147.
- [37] H.-J. Chang, M. Fivel, D. Rodney, M. Verdier, Multiscale modelling of indentation in FCC metals: From atomic to continuum, Comptes Rendus Physique 11 (2010) 285-292. URL: https://www.sciencedirect.com/

- science/article/pii/S1631070510000721. doi:10.1016/j.crhy.2010.07.007, number: 3.
- [38] C. Zambaldi, D. Raabe, Plastic anisotropy of -TiAl revealed by axisymmetric indentation, Acta Materialia 58 (2010) 3516-3530. URL: https://www.sciencedirect.com/science/article/pii/S1359645410001114. doi:10.1016/j.actamat.2010.02.025, number: 9.
- [39] C. Zambaldi, Y. Yang, T. R. Bieler, D. Raabe, Orientation informed nanoindentation of -titanium: Indentation pileup in hexagonal metals deforming by prismatic slip, Journal of Materials Research 27 (2012) 356– 367. URL: https://doi.org/10.1557/jmr.2011.334. doi:10.1557/jmr. 2011.334, number: 1.
- [40] W. Z. Yao, J. H. You, Berkovich nanoindentation study of monocrystalline tungsten: a crystal plasticity study of surface pile-up deformation, Philosophical Magazine 97 (2017) 1418–1435. URL: https://www.tandfonline.com/doi/full/10.1080/14786435.2017.1299237. doi:10.1080/14786435.2017.1299237, number: 17.
- [41] Y. Zhou, Q. Fan, X. Liu, D. Wang, X. Zhu, Experimental study and crystal plasticity finite element simulations of nano-indentation-induced lattice rotation and the underlying mechanism in TC6 single -grain, Materials & Design 188 (2020) 108423. URL: https://www.sciencedirect.com/science/article/pii/S0264127519308615. doi:10.1016/j.matdes.2019.108423.
- [42] A. Mozafari, B. Fu, D. Chalapathi, H. Abdolvand, Characterization of IN738LC using in situ nanoindentation and crystal plasticity modeling, Materials & Design 257 (2025) 114378. URL: https://www.sciencedirect.com/science/article/pii/S0264127525007981. doi:10.1016/j.matdes.2025.114378.
- [43] J. Alkorta, J. Martínez-Esnaola, J. G. Sevillano, Absence of one-to-one correspondence between elastoplastic properties and sharp-indentation load-penetration data, Journal of Materials Research 20 (2005) 432–437. URL: http://link.springer.com/10.1557/JMR.2005.0053. doi:10.1557/JMR.2005.0053, number: 2.
- [44] T. W. Capehart, Y.-T. Cheng, Determining constitutive models from conical indentation: Sensitivity analysis, Journal of Materials Research 18 (2003) 827-832. URL: http://link.springer.com/10.1557/JMR.2003.0113. doi:10.1557/JMR.2003.0113, number: 4.
- [45] O. Casals, J. Alcalá, The duality in mechanical property extractions from Vickers and Berkovich instrumented indentation experiments, Acta Materialia 53 (2005) 3545-3561. URL: https://linkinghub.elsevier. com/retrieve/pii/S1359645405002181. doi:10.1016/j.actamat.2005. 03.051, number: 13.
- [46] K. Tho, S. Swaddiwudhipong, Z. Liu, K. Zeng, J. Hua, Uniqueness of reverse analysis from conical indentation tests, Journal of Materials Research 19 (2004) 2498–2502. URL: http://link.springer.com/10.1557/ JMR.2004.0306. doi:10.1557/JMR.2004.0306, number: 8.

- [47] Y.-T. Cheng, C.-M. Cheng, Can stress—strain relationships be obtained from indentation curves using conical and pyramidal indenters?, Journal of Materials Research 14 (1999) 3493—3496. URL: http://link.springer.com/10.1557/JMR.1999.0472. doi:10.1557/JMR.1999.0472, number: 9.
- [48] V. Fauvel, Y. Gaillard, R. Guillemet, P. Garabédian, F. Richard, Simultaneous extraction of the elastic-plastic properties of a thin film and its substrate from an identifiability-based design of depth-sensing nanoindentation testing, Journal of the Mechanics and Physics of Solids 163 (2022) 104860. URL: https://linkinghub.elsevier.com/retrieve/pii/S0022509622000722. doi:10.1016/j.jmps.2022.104860.
- [49] D. Esqué-de Los Ojos, J. Očenášek, J. Alcalá, Sharp indentation crystal plasticity finite element simulations: Assessment of crystallographic anisotropy effects on the mechanical response of thin fcc single crystalline films, Computational Materials Science 86 (2014) 186–192. URL: https://linkinghub.elsevier.com/retrieve/pii/S0927025614000822. doi:10.1016/j.commatsci.2014.01.064.
- [50] A. Bourceret, A. Lejeune, Y. Gaillard, F. Richard, On the interest of the Berkovich and conical tip shape to identify interactions between dislocations in nickel single crystals from the residual to-pography, in: Indentation 2021, Lorient, France, 2021. URL: https://hal.science/hal-03456155.
- [51] L. Méric, P. Poubanne, G. Cailletaud, Single Crystal Modeling for Structural Calculations: Part 1—Model Presentation, Journal of Engineering Materials and Technology 113 (1991) 162-170. URL: https://asmedigitalcollection.asme.org/materialstechnology/article/ 113/1/162/402562/Single-Crystal-Modeling-for-Structural. doi:10.1115/1.2903374, number: 1.
- [52] H. Haddou, Influence de la taille de grain et de l'énergie de défaut d'empilement sur l'état de contraintes internes développé au cours de la déformation plastique en traction simple et en fatigue oligocyclique (Alliages C. F. C.), PhD Thesis, 2003. URL: http://www.theses.fr/ 2003COMP1444.
- [53] F. Bachmann, R. Hielscher, H. Schaeben, Texture Analysis with MTEX Free and Open Source Software Toolbox, Solid State Phenomena 160 (2010) 63-68. URL: https://www.scientific.net/SSP.160.63. doi:10.4028/www.scientific.net/SSP.160.63.
- [54] F. Bachmann, R. Hielscher, H. Schaeben, Grain detection from 2d and 3d EBSD data—Specification of the MTEX algorithm, Ultramicroscopy 111 (2011) 1720-1733. URL: https: //www.sciencedirect.com/science/article/pii/S0304399111001951. doi:10.1016/j.ultramic.2011.08.002, number: 12.
- [55] G. Nolze, R. Hielscher, Orientations perfectly colored, Journal of Applied Crystallography 49 (2016) 1786–1802. URL: http://scripts.iucr.org/ cgi-bin/paper?S1600576716012942. doi:10.1107/S1600576716012942, number: 5.

- [56] I. Horcas, R. Fernández, J. Gómez-Rodríguez, J. Colchero, J. Gómez-Herrero, A. Baro, WSXM: A software for scanning probe microscopy and a tool for nanotechnology, Review of Scientific Instruments 78 (2007). doi:10.1063/1.2432410, number: 1.
- [57] E. H. Lee, Elastic-Plastic Deformation at Finite Strains, Journal of Applied Mechanics 36 (1969) 1–6. URL: https://doi.org/10.1115/1.3564580. doi:10.1115/1.3564580, number: 1.
- [58] J. Mandel, Generalisation de la theorie de plasticite de W. T. Koiter, International Journal of Solids and Structures 1 (1965) 273-295. URL: https://linkinghub.elsevier.com/retrieve/pii/002076836590034X. doi:10.1016/0020-7683(65)90034-X, number: 3.
- [59] E. Schmid, W. Boas, Plasticit of crystals, with special reference to metals, Chapman & Hall, 1968.
- [60] J. Lemaitre, J.-L. Chaboche, A. Benallal, R. Desmorat, Mécanique des matériaux solides, Dunod, Paris, 2009.
- [61] M. Idriss, O. Bartier, G. Mauvoisin, X. Hernot, A phenomenological study of the influence of the hardening type on the indentation F-h cyclic curve, International Journal of Mechanical Sciences 197 (2021) 106336. URL: https://linkinghub.elsevier.com/retrieve/pii/S0020740321000710. doi:10.1016/j.ijmecsci.2021.106336.
- [62] R. Madec, L. P. Kubin, Dislocation strengthening in FCC metals and in BCC metals at high temperatures, Acta Materialia 126 (2017) 166-173. URL: https://linkinghub.elsevier.com/retrieve/pii/S1359645416309764. doi:10.1016/j.actamat.2016.12.040.
- [63] P. Franciosi, Etude théorique et expérimentale du comportement élastoplastique des monocristaux métalliques se déformant par glissement: modélisation pour un chargement complexe quasi statique, PhD Thesis, 1984. Publication Title: These de Doctorat d'Etat, Université Paris Nord-Paris XIII.
- [64] R. Madec, C. Denoual, J.-L. Dequiedt, A. Masson, Calibration du modèle de Teodosiu par approche multiéchelle (2019) 10. URL: https://cfm2019. sciencesconf.org/259070.html.
- [65] T. Helfer, A. Bourceret, A. Lejeune, How to implement the Méric-Cailletaud single crystal behaviour using MFront, 2020. doi:10.13140/RG. 2.2.26414.43840.
- [66] A. Bourceret, Identification des coefficients d'interaction entre les systèmes de glissement d'un cristal CFC par analyse inverse à partir d'empreintes de nanoindentation Berkovich, PhD Thesis, 2024. URL: http://www.theses. fr/2024UBFCD012/document.
- [67] J. C. Simo, T. A. Laursen, An augmented lagrangian treatment of contact problems involving friction, Computers & Structures 42 (1992) 97-116. URL: https://www.sciencedirect.com/science/article/pii/ 004579499290540G. doi:10.1016/0045-7949(92)90540-G, number: 1.

- [68] K. J. Bathe, Finite Element Procedures, upper saddle river,nj: prentice-hall ed., 1996. URL: \protect\begingroup\immediate\write\@unused\def\MessageBreak \let\protect\edefYoumayprovideadefinitionwith\MessageBreak\DeclareUnicodeCharacter\errhelp\let\def\MessageBreak \def\errmessageLaTeXError:Unicodecharacter\arta\delta(U+200E)\MessageBreaknotsetupforusewithLaTeX.

  'SeetheLaTeXmanualorLaTeXCompanionforexplanation.

  'TypeH<return>forimmediatehelp\endgroup978-0133014587.
- [69] M. Fivel, S. Forest, Plasticité cristalline et transition d'échelle : cas du polycristal, Étude et propriétés des métaux (2004). URL: https://www.techniques-ingenieur.fr/doi/10.51257/a/v1/m4017. doi:10.51257/a-v1-m4017.
- [70] M. Kraska, M. Doig, D. Tikhomirov, D. Raabe, F. Roters, Virtual material testing for stamping simulations based on polycrystal plasticity, Computational Materials Science 46 (2009) 383-392. URL: https:// linkinghub.elsevier.com/retrieve/pii/S0927025609001256. doi:10. 1016/j.commatsci.2009.03.025, number: 2.
- [71] E. Renner, Vers l'identification d'une loi de plasticité monocristalline par analyse topographique d'empreintes de nanoindentation Berkovich, Thèse, Université de Franche-Comté, 2016. URL: https://tel.archives-ouvertes.fr/tel-01652133.
- [72] K. T. Kavanagh, R. W. Clough, Finite element applications in the characterization of elastic solids, International Journal of Solids and Structures 7 (1971) 11-23. URL: https://www.sciencedirect.com/science/article/pii/0020768371900151. doi:10.1016/0020-7683(71) 90015-1, number: 1.
- [73] M. Bocciarelli, G. Bolzon, G. Maier, Parameter identification in anisotropic elastoplasticity by indentation and imprint mapping, Mechanics of Materials 37 (2005) 855-868. URL: https://linkinghub.elsevier. com/retrieve/pii/S0167663604001280. doi:10.1016/j.mechmat.2004. 09.001, number: 8.
- [74] G. Bolzon, V. Buljak, G. Maier, B. Miller, Assessment of elastic-plastic material parameters comparatively by three procedures based on indentation test and inverse analysis, Inverse Problems in Science and Engineering 19 (2011) 815-837. URL: https://www.tandfonline.com/doi/full/ 10.1080/17415977.2011.551931. doi:10.1080/17415977.2011.551931, number: 6.
- [75] F. Richard, Identification du comportement et évaluation de la fiabilité des composites stratifiés (1999). URL: https://fabricerichard.github.io/ MIC2M\_web/.
- [76] F. Richard, Vers une détermination guidée par l'identifiabilité du comportement mécanique des matériaux par nanoindentation, Habilitation à diriger des recherches, COMUE Université Bourgogne Franche-Comté, 2017. URL: https://hal.archives-ouvertes.fr/tel-01590429.

- [77] X. Chen, N. Ogasawara, M. Zhao, N. Chiba, On the uniqueness of measuring elastoplastic properties from indentation: The indistinguishable mystical materials, Journal of the Mechanics and Physics of Solids 55 (2007) 1618-1660. URL: https://linkinghub.elsevier.com/retrieve/pii/S0022509607000245. doi:10.1016/j.jmps.2007.01.010, number: 8.
- [78] K. Levenberg, A Method for the Solution of Certain Non-Linear Problems in Least Squares, Quarterly of Applied Mathematics 2 (1944) 164–168. URL: https://www.jstor.org/stable/43633451, number: 2 Publisher: Brown University.
- [79] D. W. Marquardt, An Algorithm for Least-Squares Estimation of Nonlinear Parameters, Journal of the Society for Industrial and Applied Mathematics 11 (1963) 431–441. URL: https://www.jstor.org/stable/2098941, number: 2 Publisher: Society for Industrial and Applied Mathematics.
- [80] P. Delobelle, F. Richard, M. Qasmi, Quelques potentialités de l'essai de nanoindentation. Cas du nickel polycristallin et électrodéposé: interprétation du module d'indentation, de la dureté, des effets d'échelle et des paramètres d'identification inverse, Matériaux & Techniques 96 (2008) 83-94. URL: http://www.mattech-journal.org/10.1051/mattech/2009006. doi:10.1051/mattech/2009006.
- [81] X. Long, Y. Li, Z. Shen, Y. Su, T. Gu, K. S. Siow, Review of uniqueness challenge in inverse analysis of nanoindentation, Journal of Manufacturing Processes 131 (2024) 1897–1916. URL: https://www.sciencedirect.com/science/article/pii/S1526612524010466. doi:10.1016/j.jmapro.2024.10.005.
- [82] J. K. Phadikar, T. A. Bogetti, A. M. Karlsson, On the uniqueness and sensitivity of indentation testing of isotropic materials, International Journal of Solids and Structures 50 (2013) 3242-3253. URL: https://www.sciencedirect.com/science/article/pii/S0020768313002412. doi:10.1016/j.ijsolstr.2013.05.028, number: 20.
- [83] F. Richard, M. Villars, S. Thibaud, Viscoelastic modeling and quantitative experimental characterization of normal and osteoarthritic human articular cartilage using indentation, Journal of the Mechanical Behavior of Biomedical Materials 24 (2013) 41–52. URL: https://linkinghub.elsevier.com/retrieve/pii/S1751616113001355. doi:10.1016/j.jmbbm.2013.04.012.
- [84] M. J. Pac, S. Giljean, C. Rousselot, F. Richard, P. Delobelle, Microstructural and elasto-plastic material parameters identification by inverse finite elements method of Ti(1x)AlxN (0, Thin Solid Films 569 (2014) 81-92. URL: https://www.sciencedirect.com/science/article/pii/S0040609014007585. doi:10.1016/j.tsf.2014.07.037.
- [85] D. N. Gujarati, Basic econometrics, 4. ed ed., McGraw Hill, Boston, Mass., 2003.

- [86] L. Tabourot, M. Fivel, E. Rauch, Generalised constitutive laws for f.c.c. single crystals, Materials Science and Engineering: A 234-236 (1997) 639-642. URL: https://www.sciencedirect.com/science/article/pii/S0921509397003535. doi:10.1016/S0921-5093(97)00353-5.
- [87] U. F. Kocks, The relation between polycrystal deformation and single-crystal deformation, Metallurgical Transactions 1 (1970) 1121–1143. URL: https://doi.org/10.1007/BF02900224. doi:10.1007/BF02900224, number: 5.
- [88] B. Devincre, T. Hoc, L. P. Kubin, Collinear interactions of dislocations and slip systems, Materials Science and Engineering: A 400-401 (2005) 182-185. URL: https://linkinghub.elsevier.com/retrieve/pii/S0921509305003333. doi:10.1016/j.msea.2005.02.071.
- [89] P. Juran, P.-J. Liotier, C. Maurice, F. Valiorgue, G. Kermouche, Investigation of indentation-, impact- and scratch-induced mechanically affected zones in a copper single crystal, Comptes Rendus Mécanique 343 (2015) 344-353. URL: https://linkinghub.elsevier.com/retrieve/pii/S163107211500042X. doi:10.1016/j.crme.2015.03.003, number: 5-6.
- [90] S. Breumier, F. Richard, C. Maurice, A. Villani, G. Kermouche, M. Lévesque, Complementarity of impact shot displacements and induced residual stress fields for a reliable estimation of crystal viscoplasticity parameters (2020). URL: https://hal.science/hal-03019130.